UNIVERSIDAD SAN FRANCISCO DE QUITO USFQ

Colegio de Posgrados

Development of a Method for Studying the Influence of Seismically Induced Geo-Electromagnetic Fields on the Detection of Secondary Cosmic Ray Fluxes at Ground Level

Proyecto de investigación

Pablo Andrés Buitrón Espinoza

Director de tesis: Edgar Fernando Carrera Jarrín, Ph.D.

Trabajo de titulación de posgrado presentado como requisito para la obtención del título de Magister en Física

Quito, 25 de abril de 2024

UNIVERSIDAD SAN FRANCISCO DE QUITO USFQ

Colegio de Posgrados

Hoja de calificación de trabajo de titulación

Development of a Method for Studying the Influence of Seismically Induced Geo-Electromagnetic Fields on the Detection of Secondary Cosmic Ray Fluxes at Ground Level

Pablo Andrés Buitrón Espinoza

Nombre del director de tesis, título académico: Edgar Fernando Carrera Jarrín, Ph.D.

Calificación: _____

Firma: _____

25 de abril de 2024

Derechos de autor

Por medio del presente documento certifico que he leído todas las Políticas y Manuales de la Universidad San Francisco de Quito USFQ, incluyendo la Política de Propiedad Intelectual USFQ, y estoy de acuerdo con su contenido, por lo que los derechos de propiedad intelectual del presente trabajo quedan sujetos a lo dispuesto en esas Políticas.

Asimismo, autorizo a la USFQ para que realice la digitalización y publicación de este trabajo en el repositorio virtual, de conformidad a lo dispuesto en el Art. 144 de la Ley Orgánica de Educación Superior.

Firma del estudiante: ————————————————

Nombres y apellidos: Pablo Andrés Buitrón Espinoza

Código: 00329375

Cédula de identidad: 1726679077

Lugar y fecha: Quito, 25 de abril de 2024

AGRADECIMIENTOS

Quiero expresar mi más sincero agradecimiento a mis padres por su inquebrantable apoyo y amor infinito, que han sido mi fuerza motriz en cada paso de este camino académico. También quiero reconocer y agradecer profundamente al profesor Edgar Carrera por su guía experta y su dedicación en la elaboración de este proyecto, su mentoría ha sido invaluable para mí.

Asimismo, deseo expresar mi gratitud al Departamento de Física de la USFQ por proporcionarme un entorno excepcional que ha contribuido significativamente a mi desarrollo profesional y personal a lo largo de mis años de estudio en la institución.

No puedo dejar de agradecer al revisor de este trabajo, Ernesto Contreras, cuya sabiduría y perspectiva han enriquecido significativamente no solo mi comprensión y enfoque en esta investigación, sino también en otros campos de conocimiento.

Finalmente, extiendo mi reconocimiento y agradecimiento a todo el personal que conforma la dirección de la maestría, cuyo apoyo constante y compromiso con la excelencia académica han sido fundamentales para mi crecimiento y éxito en este programa de posgrado.

Resumen

Este estudio investiga la influencia de los campos geo-electromagnéticos inducidos por sismos en la detección de partículas secundarias en la superficie terrestre. Nuestro enfoque integra diversos marcos de software, como Corsika, ARTI, Geant4 y Docker, junto con parámetros clave y análisis inicial del flujo de partículas. A través de simulaciones, identificamos restricciones relacionadas con la distancia y la altitud de la zona afectada por los campos electromagnéticos. Descubrimos que la extensión de los tiempos de simulación mejoró la generación de datos, y la optimización de los parámetros de Geant4 mejoró significativamente la confiabilidad de los resultados. La implementación de flujos de trabajo optimizados y contenedores Docker aumentó notablemente la productividad de la investigación. Estos hallazgos subrayan el papel crítico de los métodos de simulación integrales y la optimización en el avance de nuestra comprensión de las interacciones de los rayos cósmicos con la atmósfera y los campos electromagnéticos.

Abstract

This study delves into the impact of seismically induced geo-electromagnetic fields on the detection of secondary particles on Earth's surface. Our approach integrates various software frameworks including Corsika, ARTI, Geant4, and Docker, alongside key parameters and initial particle flux analysis. Through simulations, we identified constraints related to the distance and altitude of the zone affected by electromagnetic fields. Extending simulation times proved beneficial in enhancing data generation, while optimizing Geant4 parameters significantly improved result reliability. The implementation of streamlined workflows and Docker containers notably augmented research productivity. These findings underscore the critical role of comprehensive simulation methods and optimization in advancing our understanding of cosmic ray interactions with the atmosphere and electromagnetic fields.

INDEX

Figure index

Chapter I

Introduction

1.1 Cosmic rays

Cosmic rays are particles originating from space that traverse the universe. Initially, they were atoms whose outer layers were stripped away, leaving only their nuclei. These particles move at incredible speeds, approaching the velocity of light [1].

Earth is bombarded by trillions of cosmic rays daily. While the majority are intercepted by the Earth's atmosphere and magnetic field, some interact with atmospheric particles, generating secondary particle showers that reach the Earth's surface.

1.1.1 Origin

The primary source of cosmic rays reaching Earth is the sun, although we also detect particles believed to originate from distant galaxies.
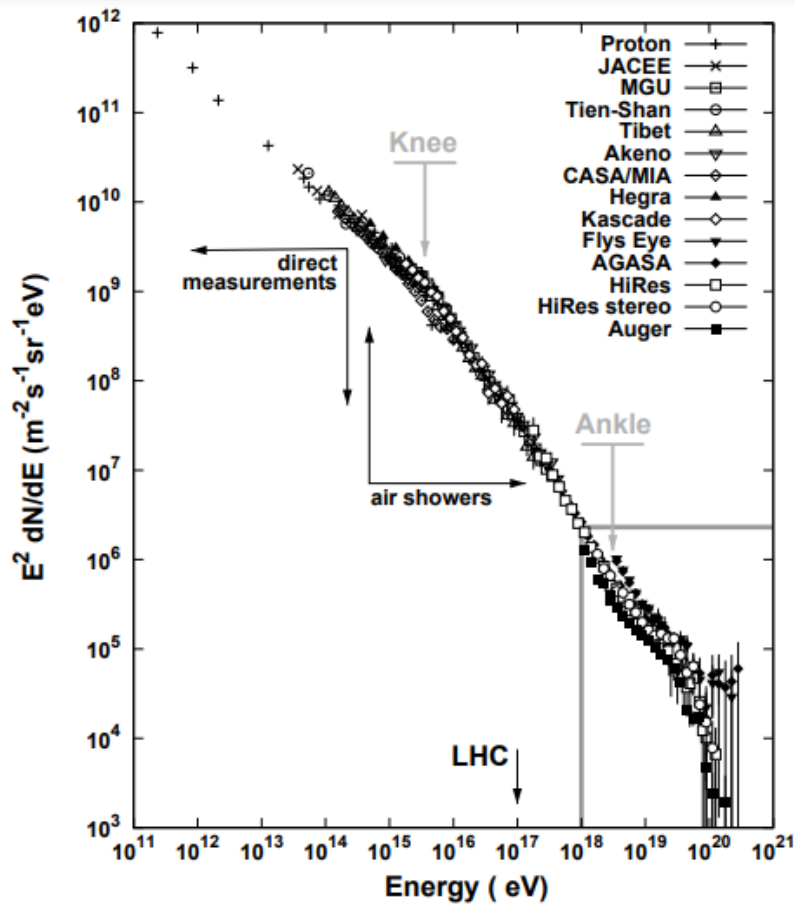
Figure 1.1: The graph illustrates the energy spectrum of cosmic rays surpassing 10^{11} eV, scaled by the square of energy (E^2). Gray arrows denote the locations of the cosmic rays' knee and ankle. It incorporates data from various contributing experiments, alongside the equivalent laboratory energy of the Large Hadron Collider. [2]

In the field of particle astrophysics, it has been observed that the energy distribution of cosmic rays (high-energy subatomic particles reaching Earth from space) is not uniform but exhibits distinctive features in the form of a "knee," "ankle," and "toe" as shown in 1.1. These abrupt changes in energy distribution are of significant interest to researchers as they provide crucial information about the sources and propagation of cosmic rays. The "knee" represents a shift in the energy distribution of cosmic rays around 10^{15} eV. Below this energy, the arrival rate

of cosmic rays increases with energy, but above this energy, the arrival rate begins to decrease. The exact cause of the knee is not fully understood, but it is believed to result from the transition from a population of galactic cosmic rays to an extragalactic population. The "ankle" is another shift in the energy distribution of cosmic rays around 10^{18} eV. Above this energy, the arrival rate of cosmic rays increases again with energy. The cause of the ankle is also a subject of debate, but it is thought to result from the transition of cosmic rays from nearby galaxies to cosmic rays from even more distant sources, such as quasars or active galactic nuclei. The "toe" is a final region in the energy distribution of cosmic rays above 10^{19} eV, where the arrival rate begins to decrease again. The cause of the toe is also debated but is believed to result from the interaction of cosmic rays with the cosmic microwave background radiation, which limits the maximum energy of particles that can propagate through space [2].

Studying cosmic rays provides insights into space and the cosmos. In the 20th century, they contributed to the discovery of antimatter and the muon, marking the first evidence of subatomic particles beyond protons, neutrons, and electrons. Additionally, cosmic rays shed light on the chemical and physical composition of the universe, its evolutionary history, and phenomena like supermassive black holes and supernovae.

The idea that supernova remnants play a significant role in accelerating galactic cosmic rays is widely accepted. This concept was initially proposed in [3], where observations of the energetics of supernova remnants formed the basis of the theory. It was argued that even a small fraction of the kinetic energy released by supernova remnants could account for the entirety of galactic cosmic rays.

One reason why supernova remnants are thought to be a prime candidate for cosmic ray acceleration is that they have higher magnetic fields than the average interstellar medium. Additionally, these remnants are large and long-lived enough to facilitate the acceleration of particles

to high energies. The mechanism for cosmic ray acceleration in supernova remnants is believed to be stochastic acceleration in supernova blast shocks.This acceleration occurs when the shock wave created by the expanding supernova remnant moves through the interstellar medium at a velocity that exceeds the sound speed of the medium. The resulting acceleration is much faster than Fermi's original acceleration mechanism, with the energy gain proportional to the velocity of the magnetic cloud or the explosion shock in terms of c, the speed of light.

The energy E is the fundamental parameter used to classify cosmic ray. Compared to the average velocity of molecular clouds, the velocity of the supernova shock is much greater. As a result, shock acceleration is significantly more efficient and faster. This theory was first proposed in the late 1970s [4] [5] [6] [7]. The predicted cosmic ray spectrum is a flat E^2 distribution in non-relativistic shock acceleration and a steeper $E^{2.2-2.3}$ in highly relativistic shock acceleration as shown in Figure1.1.

1.1.2 Cosmic rays interaction with the atmosphere

Primary cosmic rays, which are energetic particles bombarding Earth from space, do not constitute a homogeneous stream of a single type. Instead, their composition exhibits surprising diversity, surpassing the simplistic depiction of a high-energy photon stream.

The predominant constituents of primary cosmic rays consist of denuded nuclei of common atoms. These de-electronized atomic cores, accounting for approximately 99% of the primary influx, have shed their surrounding electrons during their extensive voyage through interstellar regions. Among these, protons, the hydrogen nuclei, prevail as the most abundant, followed by helium nuclei, known as alpha particles in radioactive decay processes.

However, the cosmic ray saga does not end with the spectrum delineated so far. The remaining 1% of primary cosmic rays comprises lone electrons. These unattached electrons bear

resemblance to beta particles, which are also outcomes of radioactive transformations. Although their numerical contribution is minor, their presence introduces an additional layer of intricacy to the primary cosmic ray panorama.

Upon entry into Earth's atmosphere, primary cosmic radiation interacts with the electrons and nuclei of atmospheric atoms and molecules, inducing alterations in their structure as they traverse the atmospheric layers. These particles undergo energy dissipation via both hadronic and electromagnetic mechanisms. High-energy hadrons colliding with atmospheric nuclei like Nitrogen and Oxygen initiate localized showers of penetrating particles, generated through the production of mesons and other secondary particles in these collisions [8].

Gamma-ray bursts (GRBs) represent a rare type of primary cosmic ray that stands out as the most energetic and brilliant explosions documented in the cosmos. These transient bursts of ultra-high-energy gamma rays unleash an astounding amount of energy within a mere 10-second interval, surpassing the total energy output of our Sun throughout its 10-billion-year existence. The genesis of GRBs is predominantly associated with the cataclysmic demise of massive stars or the collision of dense objects like neutron stars.

When a massive star exhausts its nuclear fuel and undergoes a catastrophic collapse, its core experiences a dramatic implosion, resulting in the ejection of a powerful jet of matter and radiation outward. This mechanism is the prevailing explanation for most GRBs. Alternatively, the merger of two neutron stars, extraordinarily dense remnants of massive stars, can also trigger a GRB as the newly formed, even denser object releases immense energy outward.

As previously noted, protons constitute the primary component of cosmic rays. These energetic particles typically undergo an average of 12 interactions as they traverse vertically through the atmosphere until reaching sea level. This creates a hadronic cascade that is the primary process of an extensive particle shower. However, most heavy nuclei in primary radiation fragment

during their first interaction, which occurs at a higher altitude than for protons due to the larger interaction cross section and the corresponding shorter mean free path of interaction. The interaction cross section between a projectile nucleus and a target nucleus scales with respect to the proton-proton interaction cross section approximately in proportion to the mass of the target nucleus.

The energy dependence of the inelastic cross section for proton-air interactions is illustrated in Figure 1.2, which shows a fit of experimental data in terms of a formula that includes logarithmic energy dependence. In summary, primary cosmic radiation undergoes complex interactions with atmospheric particles, creating extensive particle showers that vary depending on the energy and mass of the incident particles.
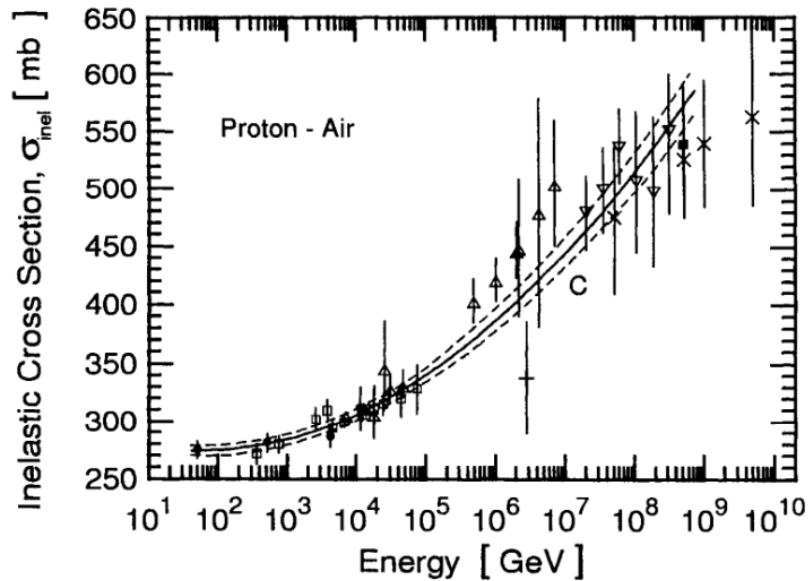
Figure 1.2: Compilation of inelastic cross sections for proton-air interactions as a function of energy ([9]; [10]). The symbols refer to the following references: •, [9]; □, [11]; △, [12]; ∇, [13]; ■, [14]; +, [15]; ×, [16].

1.1.3 Energy transport

The hadronic component of the cosmic ray shower, which is usually the principal component, plays a crucial role in our understanding of high-energy interactions in the atmosphere and energy transport. As hadrons travel through a medium, they experience energy losses due to strong interactions during collisions with nucleons and nuclei. The total hadronic cross section, σ_{tot}, is a measure of these interactions and is the sum of the elastic and inelastic parts, σ_{el} and σ_{inel}, respectively. The inelasticity, k, is also an important factor.

If a hadron with initial energy E_0 undergoes n interactions with an average inelasticity of $\langle k \rangle$, then it will retain an energy E, with $E = E_0(1 - \langle k \rangle)^n$, on average.

Collisions initiated by nucleons (p, n) and antinucleons $(\overline{p}, \overline{n})$ tend to be highly elastic, meaning the incident nucleon or antinucleon retains a relatively large fraction ($\approx 50\%$) of its initial energy upon exiting a collision. This is known as the leading particle effect. At energies below 100 GeV, annihilation of antinucleons should also be taken into account.

For a vertically incident high-energy proton traversing the entire atmosphere down to sea level, with $\langle k \rangle = 0.5$ and $n = 12$, the proton's energy is reduced by a factor of $\dfrac{E}{E_0} = (0.5)^{12} \simeq 2.5 \cdot 10^{-4}$. The leading particle effect is also observed for pions and kaons, although it is less pronounced. Interactions initiated by mesons are generally more inelastic than those initiated by nucleons or antinucleons.

High-energy interactions in the realm of strong forces and electromagnetic phenomena, like pair generation, result in the generation of subsequent particles. These include charged pions, less common kaons, various mesons, hyperons, and nucleon-antinucleon pairs formed through the vigorous interactions of energetic primary particles with the atomic nuclei in the atmosphere. Among these secondary particles, pions (π^+, π^-, π^0) are the most prevalent. In cases where these energetic secondary hadrons possess sufficient energy, they can initiate additional

hadronic interactions, spawn further secondary particles, and contribute to the formation of a hadron cascade that underpins extensive air showers. Nonetheless, it is important to note that unstable particles like pions, kaons, and others are also susceptible to decay processes [17].

Chapter II

Geoelectromagnetic interactions

This section delves into the intricate interplay between electric and magnetic fields and their effects on particle showers, with a focus on cosmic ray propagation and seismic phenomena. It begins by examining the impact of atmospheric electric fields on high-energy particle showers, emphasizing Monte Carlo simulations' role in elucidating these interactions. Additionally, it discusses the mechanisms underlying seismically induced electric and magnetic fields, highlighting their significance in earthquake prediction and understanding seismic wave dynamics.

2.1 Effects of electric fields on particle showers

The pivotal role played by atmospheric electric fields in the propagation of air showers generated by high-energy particles has been investigated through Monte Carlo simulations, as documented in [18]. These fields can significantly alter the trajectories of charged particles within the shower, influencing the energy distribution and overall shape of the shower.

The simulation model, developed using Corsika software, meticulously incorporates the

effects of electric fields on charged particles within the shower, including electrons, positrons, muons, and charged hadrons.

The primary focus of the study is on understanding the impact of atmospheric electric fields on the evolution of cosmic ray air showers, particularly emphasizing the electromagnetic aspect. It reveals that robust electric fields, similar to those in thunderstorms, can significantly affect the energy distribution of electrons and positrons within air showers. These findings are crucial for radio detection of air showers, as radio emissions depend on the behavior of these particles.

Furthermore, the article in [18] explores how air showers could trigger runaway electron breakdown in thunderstorm fields, potentially contributing to lightning initiation. This highlights the importance of integrating electric field considerations into air shower simulations for a comprehensive understanding of their behavior.

Regarding studies involving electric field variations within Corsika, these adjustments were made by globally modifying field values and toggling effects on and off at varying intensities directly within Corsika's subroutine code.

2.1.1   Seismically induced electric fields

Seismic waves generated by earthquakes can induce electric fields in the Earth's atmosphere and crust. These electric fields have been detected and studied by seismologists and geophysicists to better understand the mechanisms behind their generation and their potential use in earthquake prediction as shown in [19].

There are several mechanisms that have been proposed to explain the generation of electric fields by seismic waves. One of the most widely accepted mechanisms is the piezoelectric effect, which occurs when certain materials, such as quartz, are subjected to stress. The stress causes the material to become polarized, resulting in the generation of an electric field.

Another mechanism is the electrokinetic effect, which occurs when the movement of fluids in the Earth's crust generates an electric field [20]. Other mechanisms that have been proposed include the streaming potential effect, the electrochemical effect, and the motional induction effect [21].

Electric fields induced by seismic waves can be detected using a variety of methods, including ground-based measurements, satellite observations, and balloon-borne instruments. Ground-based measurements typically involve the use of electric field meters, which measure the electric field strength at a given location. Satellite observations can provide a global view of the electric field distribution in the Earth's atmosphere, while balloon-borne instruments can provide high-altitude measurements of the electric field [22].

Numerous studies have been conducted on electric fields induced by seismic waves, with the aim of better understanding the mechanisms behind their generation and their potential use in earthquake prediction. One study found that electric fields induced by seismic waves could be used to predict the magnitude and location of earthquakes [23].

Another study found that electric fields induced by seismic waves could be used to detect the presence of fluids in the Earth's crust, which can be an indicator of potential earthquake activity [24].

2.2   Effects of magnetic fields on particle showers

Magnetic fields play a pivotal role in shaping the trajectories and behaviors of charged particles, including cosmic rays, as they propagate through space. These fields can significantly influence the paths and energies of particles, leading to intricate phenomena such as particle deflection, confinement, and acceleration. For instance, the magnetic field of the Sun, known as the solar

magnetic field, interacts with charged particles emitted during solar flares and coronal mass ejections, directing them along magnetic field lines and contributing to the dynamics of space weather [25]. In interstellar space, the magnetic fields within galaxies, such as the Milky Way's magnetic field, affect the propagation of cosmic rays over vast distances, influencing their arrival patterns and energy spectra observed by detectors on Earth [26].

Closer to home, Earth's magnetic field exerts a profound impact on cosmic ray showers. The magnetosphere, a region of space influenced by Earth's magnetic field, deflects and traps charged particles from the solar wind, shielding the planet's surface from the majority of low-energy cosmic rays. However, high-energy cosmic rays, especially those with ultra-high energies, can penetrate the magnetosphere and interact with the Earth's atmosphere, initiating extensive air showers and producing secondary particles that can be detected by ground-based observatories. Understanding the complex interplay between magnetic fields and cosmic ray propagation is essential for unraveling the mysteries of cosmic ray origins, acceleration mechanisms, and their effects on Earth's environment and space weather [27].

2.2.1 Seismically induced magnetic fields

Seismic activity can induce magnetic fields in the Earth's atmosphere, which can impact the detection of cosmic rays. The mechanism by which seismic activity induces magnetic fields is not well understood, but it is thought to be related to the piezomagnetic effect in rocks [28]. Several studies have reported an increase in the flux of cosmic rays during and after earthquakes, which has been attributed to the induction of magnetic fields by seismic activity [29].

When seismic waves propagate in the conducting crust, they will make the crust material move and cut the geomagnetic field and cause magnetic field vibrations [29]. This is known as the motional induction effect, which is an effective mechanism to generate earthquake-induced

electromagnetic (EM) fields [28]. The motional induction effect is based on Faraday's law of electromagnetic induction, which states that a changing magnetic flux induces an electric field. In the case of seismic waves, the motion of the Earth's crust induces a changing magnetic field, which in turn induces an electric field. This electric field can then induce a magnetic field, resulting in the generation of earthquake-induced EM fields[28].

The piezomagnetic effect is another mechanism that has been proposed to explain the induction of magnetic fields by seismic waves. This effect is based on the fact that some rocks have magnetic properties that are sensitive to stress. When rocks are subjected to stress, they can become magnetized, resulting in the generation of a magnetic field [19].

Rotation of coil-type magnetometers caused by seismic waves can change the magnetic flux of the Earth's magnetic field through the coils and thereby give rise to rotation-induced magnetic fields (RIMFs), which have contribution to so-called coseismic magnetic disturbances during earthquake events [30].

Chapter III

Simulation infrastructure

3.1   Primary software tools

In our ongoing investigation, as outlined earlier, our primary focus lies on elucidating the influence of geo-electromagnetic fields on the detection mechanisms of cosmic rays at ground level. This required employing advanced simulation tools to precisely model and analyze these complex interactions. After careful consideration and evaluation, we identified specific software as indispensable for the successful execution of our study. These software tools serve as the linchpin of our research endeavor, providing the essential framework for data generation, analysis, and interpretation. In this section, we will delve into a detailed introduction of these pivotal software components, highlighting their functionalities, capabilities, and relevance to our investigative pursuits.

Corsika

Corsika, short for Cosmic Ray Simulation for Kascade, is a versatile software package designed to simulate high-energy cosmic rays' interactions within Earth's atmosphere. Widely utilized in astroparticle physics, Corsika allows researchers to delve into cosmic ray properties and their interactions with matter across a broad energy spectrum, ranging from 100 MeV to 10 EeV. Developed initially in the 1990s by a team from the Karlsruhe Institute of Technology in Germany [31], Corsika has since undergone continuous refinement and enhancement, incorporating new functionalities and capabilities.

Today, Corsika stands as a cornerstone simulation tool within the astroparticle physics community, employed globally by researchers to explore cosmic ray characteristics and their intricate interactions with atmospheric elements. One of its standout features lies in its capacity to meticulously model extensive air showers (EAS) triggered by cosmic ray interactions in the atmosphere. EAS represent intricate cascades of particles resulting from high-energy cosmic rays entering Earth's atmosphere and interacting with air molecules. Corsika's capability to simulate the complete evolution of these showers, from their inception through atmospheric interactions to ground-level particle detection, renders it indispensable for probing cosmic ray properties and their interplay with matter.

ARTI

The LAGO (Latin American Giant Observatory) project [32], led by a collaborative network of over 90 scientists from more than 25 institutions across 9 Latin American countries and Spain, is a significant initiative in Astroparticle physics research. It focuses on studying the Extreme Universe, Space Weather phenomena, and Atmospheric Radiation at ground level.

As part of its research initiatives, LAGO developed the ARTI (Astroparticle Research Toolkit

and Infrastructure) software [33]. ARTI represents a comprehensive framework meticulously crafted for simulating signals generated by secondary particles resulting from the interaction of individual, multiple, or the entire spectrum of primary cosmic rays with the Earth's atmosphere. These simulated signals can be tailored for any particle detector situated at varying locations known as LAGO sites (latitude, longitude, and altitude), accounting for real-time atmospheric, geomagnetic, and detector conditions. This software, created by the collaborative efforts of LAGO's scientific network, serves as a crucial tool for analyzing data, modeling astroparticle interactions, and facilitating research in various aspects of astroparticle physics.

Constructed through a series of scripts written in C++, Fortran, and Perl, ARTI seamlessly integrates three distinct simulation environments: Magneto Cosmics, Corsika, and Geant4. These integrated tools assess the impact of the geomagnetic field on the primary cosmic ray flux, simulate atmospheric showers induced by cosmic rays, and model the response of detectors to the ensuing secondary particle flux generated within the atmosphere.

ARTI extends its functionality to compute the flux of anticipated signals resulting from sudden occurrences of gamma-ray bursts or emanating from persistent gamma sources. Furthermore, it facilitates a comparative analysis of these fluxes against the expected background, enabling the identification of such phenomena in a singular water Cherenkov detector (WCD).

Moreover, ARTI empowers precise calculations of the anticipated flux of highly energetic muons and other secondary particles at ground level. This capability allows for the injection of these particles over geological structures, particularly valuable in applications related to muography.

Geant4

Geant4 is a versatile software toolkit widely employed for the simulation of the passage of particles through matter. Developed at CERN, it has found applications in various scientific domains, including high-energy physics, medical physics, and space science. Geant4 utilizes a modular architecture, allowing users to customize simulations according to their specific requirements, and employs a range of physics models to describe particle interactions. The toolkit has become a fundamental tool in experimental and theoretical research, providing a reliable platform for simulating complex particle interactions in diverse environments [34].

One of the key strengths of Geant4 lies on its comprehensive set of physics models, which accurately describe particle interactions over a wide energy range. These models are continuously refined and validated against experimental data to ensure their accuracy and reliability. Additionally, Geant4 incorporates a flexible geometry description that enables the representation of complex experimental setups and detector configurations within what are called Geant4 *worlds*. These worlds serve as the simulated physical space where all the setup is done. Researchers and scientists leverage Geant4's capabilities to design and optimize experiments, interpret results, and enhance our understanding of fundamental physical processes [35].

Geant4 has been pivotal in advancing research across various disciplines. In the realm of medical physics, for instance, it has played a crucial role in the development of innovative imaging and treatment techniques, providing a virtual platform for testing and optimizing medical devices and procedures. Its widespread adoption across scientific communities underscores its significance and the impact it has had on advancing our knowledge of particle interactions and their implications in diverse fields [36].

3.2   Electric and magnetic fields parameters in Corsika

In the Corsika program, there is a feature called `EFIELD` that considers the impact of electric fields on the path of charged particles during the cascade. The behavior of the charged particle depends on the orientation of the electric field with respect to the particle's direction of motion, which can result in the particle being redirected, sped up, or slowed down. The `EFIELD` option is crucial for examining how charged particles interact with electric fields in the atmosphere, as this interaction can considerably affect the cascade's propagation and the particles' energy distribution.

Corsika includes the `elfield.c` file, which defines the functional dependence of the electric field intensity on the space coordinates. This subroutine must be written in C language and is used together with the Corsika program to simulate atmospheric particle cascades. A subroutine with no electric field is provided as an example, allowing the user to model their own electric field.

To modify the subroutine, only a text editor is required. When setting up and installing the Corsika program, the `elfield.c` subroutine is automatically compiled and linked to the program if the `EFIELD` option is selected.

When calling the `elfield.c` subroutine from the `ELECTR` subroutine, input variables x, y, and z are passed, representing the position at which the electric field components will be calculated. The x and y variables refer to the intersection of the cascade axis with the lowest observation level, while the zero point of the z coordinate is defined at sea level.

The `elfield.c` subroutine returns the components of the electric field intensity vector in V/cm. The user can define any functional form of the dependence of the electric field intensity on the space coordinates.

Note that the electric field in the atmosphere is generally due to weather conditions, light-

ning storms, etc. Therefore, the electric field does not extend to the stratosphere. If an electric field is defined in the `elfield.c` subroutine, the user is responsible for ensuring that there is no electric potential difference between the top of the atmosphere (where the primary particle enters the atmosphere) and ground level. Additionally, if the electric field extends to the edge of the atmosphere, unreal avalanche processes can occur in the early stages of cascade development due to excessive energy gain.

When it comes to modifications of magnetic fields in Corsika, the software provides some capabilities but with limitations. Corsika allows for basic modifications to the Earth's magnetic field, such as setting a specific strength and direction for the magnetic field at the simulation site. However, Corsika is not designed to simulate detailed and complex magnetic field structures or dynamic changes in magnetic fields over time [37].

For more detailed and dynamic simulations involving magnetic fields, researchers often integrate Corsika with other software packages or tools that specialize in magnetic field simulations. This integration allows for more accurate and comprehensive studies of particle propagation and interactions in realistic magnetic field environments. Geant4, for instance, is commonly used alongside Corsika for simulations involving electromagnetic and magnetic fields due to its robust capabilities in handling such interactions [31].

In this study, we delved into an alternative strategy aimed at resolving the specific challenge posed by the complexity and rigidity of the code files and limitations discussed earlier, particularly those pertaining to the modeling of electromagnetic (EM) fields within Corsika. The intricacies lie on the detailed analysis of how electric and magnetic fields impact particle behavior, presenting a formidable obstacle to customization according to our specific research needs. To address this intricacy comprehensively, we adopted a meticulous approach, breaking down each proposed modification into distinct phases for thorough examination and implementation,

as elaborated below.

Our simulation of the required flux time was conducted using Corsika. However, we decided against using Corsika to model changes in electromagnetic (EM) fields due to the difficulty of modifying the code related to electromagnetic interactions as desired. Instead, we employed Geant4, a particle simulation software known for its capabilities in modeling EM interactions in specific geometries. This decision was grounded in the need for a more precise and specialized tool for studying the local and specific effects of electric and magnetic fields on particles.

3.3   Electric and magnetic fields parameters in Geant4

Geant4 serves as a versatile toolkit for simulating particle interactions within matter, offering capabilities to describe and propagate particles in diverse fields such as magnetic, electric, electromagnetic, and gravitational fields [38]. Specifically focusing on electric and magnetic fields in Geant4, these parameters can be meticulously defined and tailored to replicate various experimental settings.

Within Geant4, magnetic fields can assume different configurations through models like uniform magnetic fields, solenoidal, toroidal, and quadrupole magnetic fields. The choice between a global or local field definition allows researchers to apply these fields universally across the entire detector geometry or restrict them to specific volumes or regions [38].

The implementation of magnetic fields in Geant4 employs the `G4MagneticField` class, equipped with methods to compute the magnetic field at specific spatial coordinates. Similarly, electric fields are definable using the `G4ElectricField` class, accommodating global or local field setups, and adjustable parameters to mirror real-world experimental conditions. The electric field description can range from mathematical equations defining electric potentials to

parameter-based representations of field strength and direction.

Particle propagation in electric and magnetic fields adheres to the governing equations of motion, solved in Geant4 through numerical methods like the Runge-Kutta and Dormand-Prince techniques. Fine-tuning simulation precision involves adjusting numerical method parameters such as step size and tolerance levels.

Our investigation transitioned from defining the simulation time for flux analysis, setting specific altitudes and electric field strengths in Geant4, to introducing field variations for studying secondary flux detection. This systematic approach aimed to ascertain relevant percentage variations, indicative of detectable effects. Ground-level detection comparisons helped evaluate flux changes induced by earthquake events, establishing causal links between seismic activity and observed effects.

By leveraging Geant4's capabilities for electromagnetic field modeling instead of Corsika, we aimed to bolster simulation precision and relevance, facilitating a thorough analysis of electric and magnetic field impacts on particle behavior. This strategic shift underpins our quest for more accurate and insightful simulations in this domain.

Chapter IV

Method

The initial approach taken in this study was to make changes to the electric and magnetic fields directly into the Corsika files that modulate these contributions. The idea was to modify the necessary parameters to introduce these variations in the simulation of secondary particles and their potential detection at ground level. However, after attempting to implement these changes directly in Corsika, it was concluded that it would not be feasible for two main reasons. The first reason is that introducing these changes in Corsika's programming involves modifying too many source files of the program, which can lead to unknown dependencies or behaviors in the program, resulting in errors and bugs. The second and most significant reason is that introducing these changes in the same region where we obtain the output of secondary particles to be detected at ground level would not result in a realistic simulation.

Since earthquakes typically occur far away from the detector, usually hundreds of kilometers from the detection zone, we aimed to introduce these EM changes locally, near the epicenter. This involves utilizing Corsika's data and incorporating Geant4 to simulate perturbations within a designated area, which we will refer to as the affected zone. This integration offers a more

accurate method for controlling and studying particle interactions within these regions, which are visually represented in Figure 4.1 and will be elaborated on in the following section.

4.1 Simulation strategy

Our ability to detect particles is constrained to those reaching the detector or its immediate vicinity per unit area and time, with trajectory information being inaccessible in our experimental setups. Despite this limitation, we can define specific regions relative to the detector for analysis.

In Corsika simulations, the number of detected particles directly correlates with the duration of the simulated shower: longer durations in a specific area result in higher particle counts, whereas shorter durations lead to fewer counted particles.

Our strategy involves simulating particle showers in Corsika, followed by counting the particles within the detection and affected zones separately. The initial count, at ground level, establishes a baseline particle flux under normal conditions, without seismic influence. The second count occurs in the affected zone, where interactions between secondary particles and electromagnetic fields take place. Our hypothesis suggests that these electromagnetic field regions extend from the epicenter to several meters or kilometers above the Earth's surface during an earthquake; this altitude is denoted by h in Figure 4.1. These EM fields are then locally simulated using a Geant4 world, as illustrated in Figure 4.1, with dimensions w for its length and $a \cdot h$ (where $0 < a < 1$) for its width. it is worth noting that the figure also demonstrates how these EM fields could manifest at any distance d from the detector; although these distances could be significantly greater and comparable to the Earth's radius R, for computational simplicity, we approximate $t \approx s \approx d$.

By segmenting simulations based on these defined zones, we can effectively analyze and compare particle interactions and flux under normal conditions versus those influenced by seismically-generated electromagnetic fields.

After simulating the particle shower in Corsika, we integrate the particles that pass through the affected area into a Geant4 environment. This Geant4 setup includes electric and/or magnetic fields, enabling us to observe the interactions of secondary particles with these fields. We anticipate trajectory changes as particles interact with these fields, aiming to understand how these alterations influence particle behavior and subsequent ground-level detection.

Our objective is to comprehend the outcome of these interactions, which may manifest as increased or decreased detection at the detector or exhibit minimal changes. This variability forms the core of our investigation, emphasizing the determination of how these interactions influence particle behavior and detection outcome without predefining expected results.

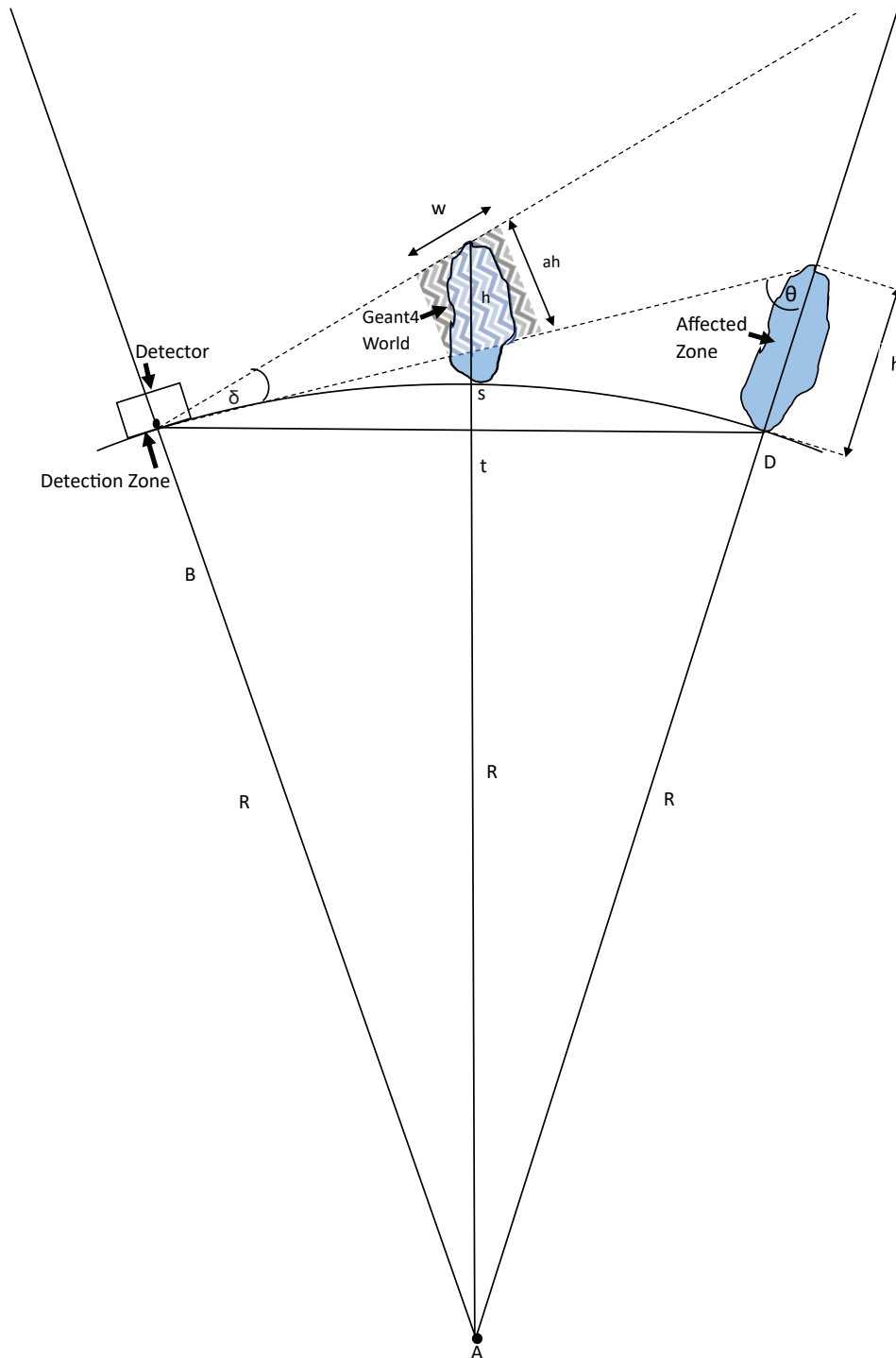Figure 4.1: This figure shows the affected and detection zones, along with the Geant4 world setup. In this context, R represents the Earth's radius, h is the altitude of the affected zone, $t \approx s \approx d$ indicates the distance to the detector, w is the length of the Geant4 world, $a \cdot h$ is its diameter, and δ and θ are the angles that define the shower boundaries.

4.2   Acquisition and data analysis

In the initial phase of data analysis for this study, the ARTI software plays a crucial role in generating the necessary data. This process involves particle data handling at the atmosphere level and at ground level following the steps shown in [33]. These particles are normalized per unit area and time, forming the basis of the dataset used for the analysis. The data obtained includes detailed information such as the position, momentum, energy, and corresponding angles of these particles, providing a comprehensive view of their behavior and characteristics.

Expanding on the previous description, the understanding of the parameters involved in this simulation is fundamental to effectively using ARTI algorithms. This includes knowledge of the height of the affected zone, the distance from the detector to the epicenter, and the duration of the event being simulated. These parameters guide the ARTI algorithms in accurately representing the particle interactions and phenomena under study. Furthermore, the choice of positioning the affected zone to the right of the detector is discussed in the context of Corsika's reference system. This decision, made without loss of generality, aligns with the northward orientation within Corsika's framework, enhancing the clarity and consistency of the simulation setup as shown in Figure 4.2. This figure also illustrates the two main fluxes to consider when discussing the particle count: the flux from what we will later define as the normal or vertical flux zone and the flux from what we will later define as the affected or horizontal flux zone.

This study addresses several critical parameters crucial for generating a diverse range of simulations. These parameters, each with their specific configurations and intervals, include the height range of the affected zone (varying from 1000 to 3000 meters above sea level), the duration of the simulated event (ranging from 1 to 3 hours), and the distance between the affected zone and the ground-based detector (spanning from 15 to 500 kilometers). The selection of these parameters is not arbitrary but based on relevant literature and scientific consensus.

The decision to use the Corsika reference system is justified by its recognized accuracy and widespread adoption within the scientific community conducting similar studies, ensuring compatibility and comparability across research endeavors.
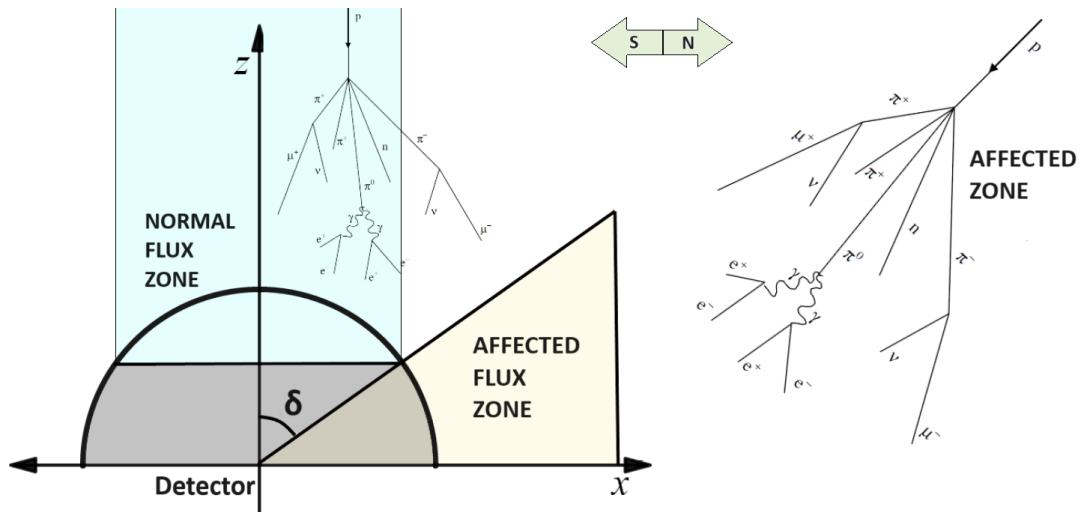
Figure 4.2: The reference system is taken from the detector. To the north of the detector is where the earthquake is said to occur, so the affected zone is indicated on the right (yellow area), while the normal flux detected is shown in the blue area

4.2.1   Definition of the key simulation parameters

Before discussing how the simulations were implemented, it is important to show the main parameters introduced in this study for further comprehension on how they impact the data generation.
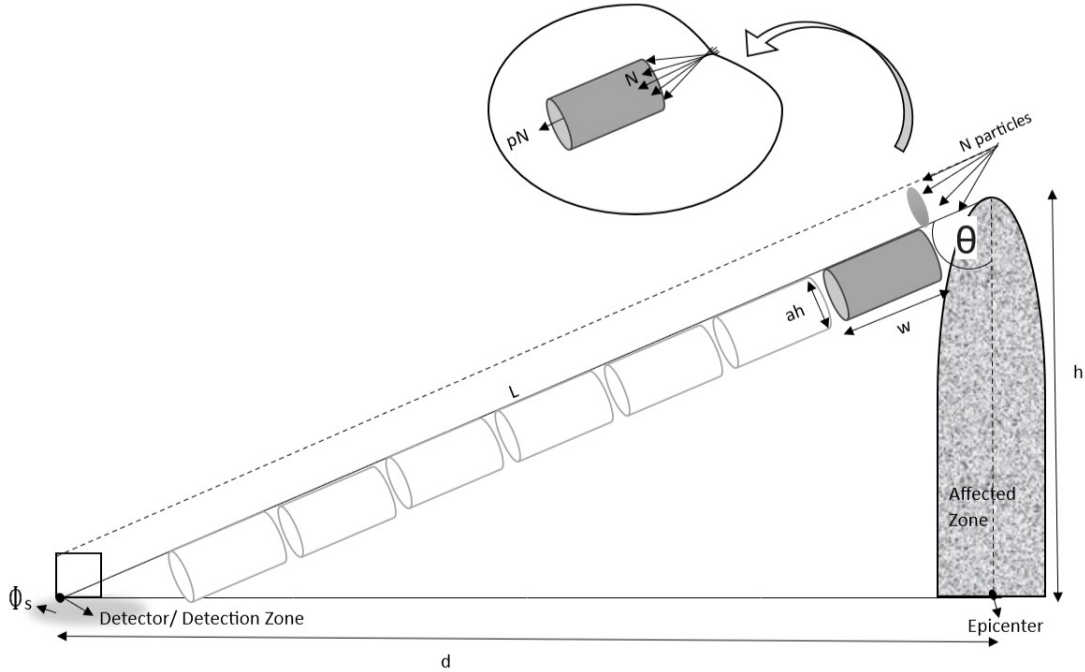
Figure 4.3: The simulation setup illustrates the detection zone, the detector, and the affected zone, along with its dimensions. The cylindrical shapes represent the Geant4 world boxes that encompass the entire particle trajectory from one zone to another.

Figure 4.3 illustrates several key parameters related to the simulation setup. On the left side, the diagram shows the detector's location, surrounded by a 1 km detection zone. The detector is situated at a distance d from the affected zone, which extends to an altitude h above the epicenter. Each shower generates N particles, traveling a length L with an inclination angle θ towards the detector.

The study of particles' interactions with the air during their travel is conducted using n cylindrical Geant4 boxes. The value of n can be determined using Equation 4.1. Each box has a diameter[1] of $a \cdot h$, where $0 < a < 1$, and a length of w. These boxes are then sequentially injected with specific ARTI particle inputs, with details on injection direction and alignment

---

[1]In this study, the area of these cylindrical boxes' caps is fixed at 1 km^2 for normalization purposes, leading to a fixed parameter $a = 1.13 \times 10^{-2}$.

to the box orientation provided in Section 4.2.3. The initial box on the right contains the total number of particles, denoted as N, while subsequent boxes receive a fraction of $p \cdot N$ due to particle-air interactions. Here, p represents the surviving fraction of particles that traverse from one end of the cylindrical box to the other.

The flux normalized in area and time, denoted as Φ_G, is determined by the total number of particles that successfully reach the detector after traversing all the cylindrical boxes. In contrast, Φ_S represents the flux counted by Corsika at ground level in the detection zone. Note that the total number of particles N depends directly on the simulated shower time t, as detailed in Annex C1.

In subsequent sections, we explore in detail how this simulation setup enables a comparison and alignment of the fluxes from Corsika and Geant4 using these parameters. it is crucial to approach this task with careful consideration; if the fluxes closely match or show reasonable similarity, it confirms the effectiveness of this simulation setup.

4.2.2   Administering particle information using ARTI

The particle table generated by ARTI serves as the final output of the Corsika simulation, containing information about every secondary particle produced during the shower. This table includes details such as the particle's position relative to the detector, its momentum components, the originating primary particle, and the identification assigned by Corsika to each distinct particle. Subsequently, we will refer to this information table simply as the shower or as the ARTI particles.

The particle table generated by ARTI after each simulation takes into account several necessary variables that must be manually input when running each algorithm. This can be done by following the steps described in [39]. However, the aim of this study is to analyze variations

in particle flux counts by assessing changes in distances, heights, times, and angles for each shower. For this reason, a script has been created to take an input with a list of parameters for each simulation and automatically output the generation of the shower, the ARTI analysis, and the filtering of particles that reach a certain distance from the detector, i.e., those that reach the detection zone after passing through the affected zone. This script is the main component of the validation method that will be discussed later. It produces, as output, the particles filtered by type that effectively manage to reach one kilometer from the detector.

To ensure a seamless analysis process, it is crucial to have all the necessary software installed on the machine or cluster being used. This can be accomplished by employing a Docker image specifically tailored for this study. In Annex A1, detailed instructions are provided for generating the table of filtered particles, extending up to one kilometer from the detector. This table, saved as a file with the extension `.shw.bz2`, represents a compressed plain-text format of the particle table using `Bzip2` compression. Importantly, this file serves as the input for the Geant4 simulation, as elaborated in the subsequent section.

4.2.3   Injecting ARTI particles into the Geant4 world

For analyzing the interaction of particles produced in the previous step with air and variations of electric and magnetic fields, Geant4 is employed. The objective here is to create a Geant4 world with the required specifications. The previously mentioned container already includes the base simulation, serving as a starting point from which parameters can be added or modified. This base simulation validates that indeed all particles or a percentage of them that passed through the affected zone reached the detection zone.
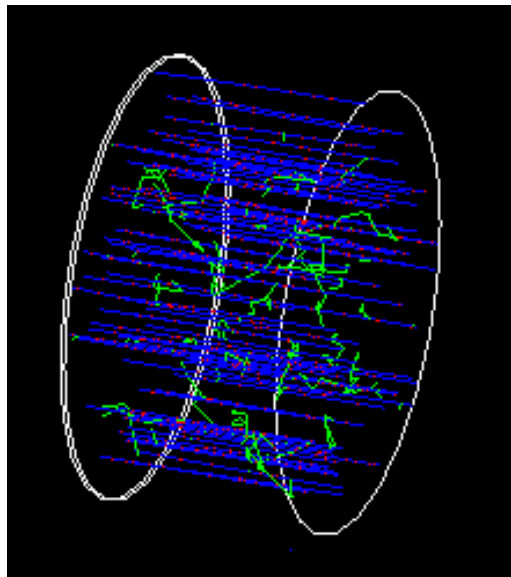
Figure 4.4: Geant4 Box showing a distribution of simulated particles. The left cap of the cylinder represents the location of the Logical detector, while the right cap signifies the point of injection for the ARTI particles.

This specific Geant4 setup, illustrated in Figure 4.4, comprises a cylindrical volume of air with adjustable length and radius based on specific requirements. In one cap of the cylinder, particle injection occurs (the input file is introduced) while detection takes place at the opposite cap. This detection is simulated with an equal volume of air; it is not a physical entity with which the particles would interact, only a logical volume that counts how many particles pass through the entire cylinder.

This cylindrical box is oriented along the primary shower direction, aligning with the z axis in the Geant4 simulation. Consequently, the injection cap of the cylinder is positioned to ensure that the collective momentum of the particles being injected aligns with the overall momentum of the shower. This alignment strategy aims to minimize the number of particles that deviate from the trajectory and remain undetected due to their divergent motion, thereby bypassing the detection zone after passing through the cylinder. The implementation of this alignment

is encapsulated within the project's constructor, detailing the specifications for creating the particle gun responsible for directing each particle through the initial cap towards the detection cap. To visualize this simulation, or any other, an environment with Geant4 installed in the suggested version and following the steps described in [40] is required. The steps to run this simulation are shown in Annex A2.

The culmination of these processes yields an analysis of particles reaching the detection zone. While the preceding section demonstrated a method to achieve this using Corsika, the introduction of the Geant4 world allows for the introduction of variations in the desired fields. Activating the electric field in the base `fsim` simulation, which can be found in [41] and detailed how to execute in Annex A2, adjusting air density, or modifying the geometry would suffice. Essentially, it is within this simulation framework that all sought-after modifications for subsequent study can be executed, incorporating field variations and subsequently correlating them with areas of affected zones generated by earthquakes.

4.3   Method validation

it is crucial to note that the two examined zones depicted in Figure 4.3 are initially disconnected. Additionally, the particle counts discussed in Section 4.1 occur at locations significantly distant from one another. The objective of the validation is to establish a connection between these regions in such a manner that ensures the particle flux remains largely unchanged as it travels from the affected zone to the detection zone.

Keep in mind that the particle shower originating from the affected zone and reaching the detection zone follows a more horizontal trajectory compared to particles arriving directly from above the detector, as shown in Figure 4.2. While this might imply an uneven distribution

between these two types of showers (mainly vertical and mainly horizontal), we conducted a simple study to discard this hypothesis. The results, presented in histograms of angular distribution and momentum distribution of particles, indicate that the particle distribution is indeed uniform, regardless of whether we are dealing with vertical or horizontal showers.

In reaching this conclusion, we undertook an analysis of the polar and azimuthal angle distributions of particles generated in both vertical and horizontal showers. The angle variables were defined according to Corsika's reference system. Specifically, the polar angle, denoted by ϕ, is measured clockwise from the north direction as defined in Figure 4.2, representing the angle on the ground plane. On the other hand, the azimuthal angle, labeled θ, is measured from Corsika's negative z direction (pointing downward) to the z-component of each particle's momentum.

Figures 4.5 and 4.6 demonstrates the uniform angular and momentum distribution observed in both vertical and horizontal showers. This observation indicates that simulating a horizontal shower extensively, despite initially having a lower particle count at ground level, tends to resemble a more vertical distribution over time. This convergence occurs due to the even distribution exhibited by particles generated in each simulation.

Similarly, Figure 4.6 demonstrates the uniform momentum distribution behavior exhibited by different types of showers.
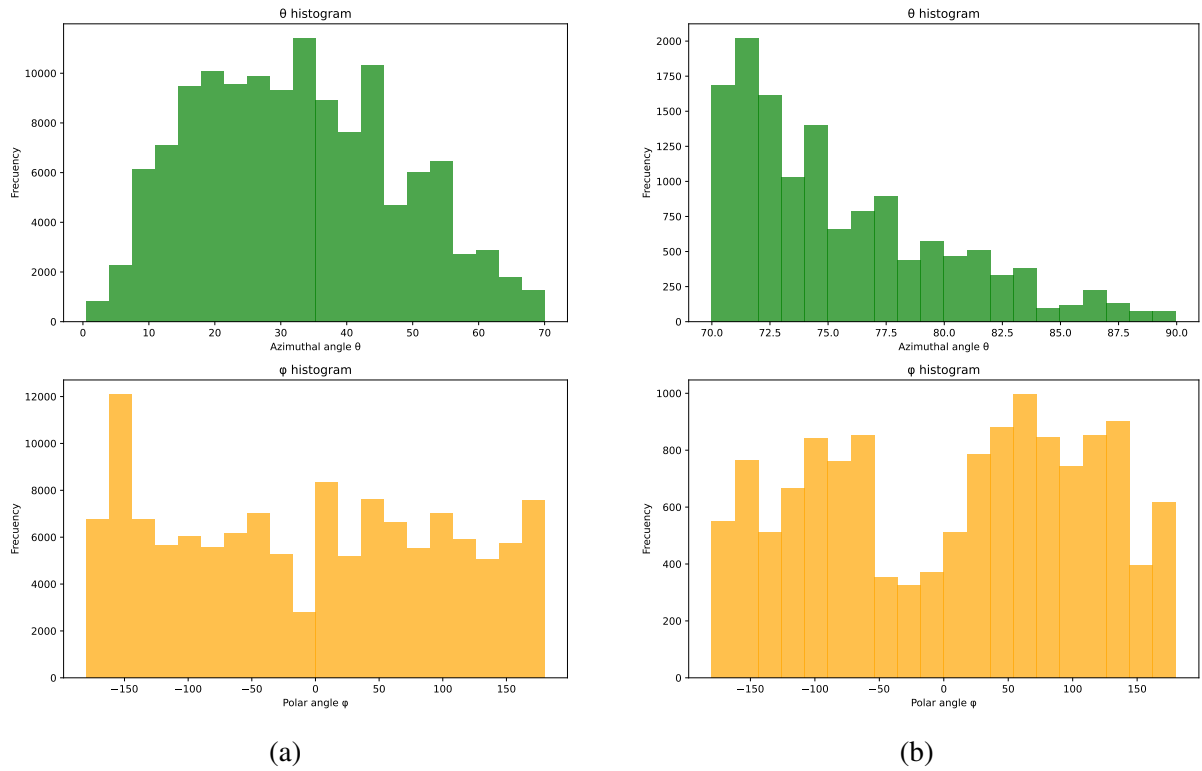
Figure 4.5: Angle distributions for two distinct types of showers: one with a predominant vertical orientation (a), and the other primarily horizontal (b)
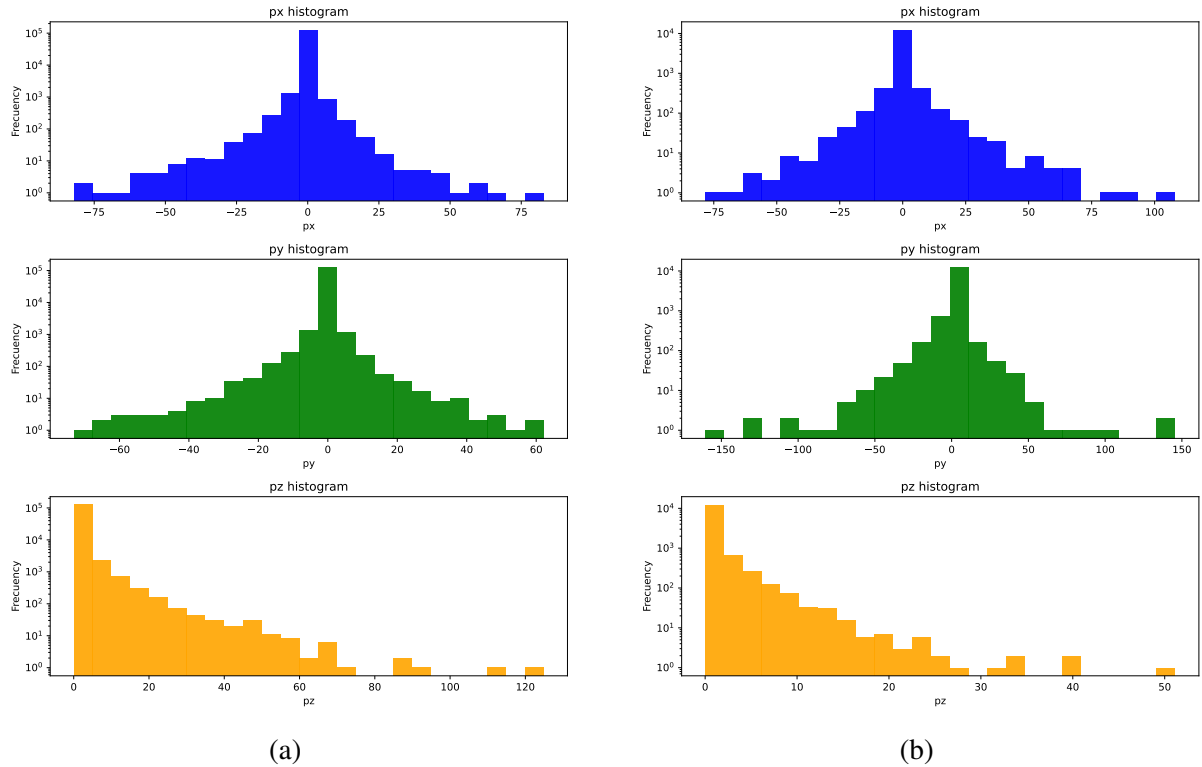
Figure 4.6: Momentum components distributions for two distinct types of showers: one with a predominant vertical orientation (a), and the other primarily horizontal (b)

After confirming that simulating more horizontal or vertical showers shows no difference, given the isotropic distribution of particles detected at ground level, we want to reiterate that what matters are the particle count and, consequently, the simulation time, rather than trajectories.

To estimate the simulation time needed for the vertical shower above the detector, representing the normal flux (without seismic influence) received by the detector, and for the horizontal shower, representing the affected flux received by the detector, it is crucial to determine the approximate number of particles arriving horizontally. The process to determine this is outlined below.

We generate a Geant4 Box as described in Section 4.2.3. The objective is to use this new Geant4 world to capture changes in the secondary detected particles, from the affected zone down to ground level, as illustrated in Figure 4.3 and further elaborated in Section 4.2.3.

As previously outlined, the strategy involves integrating a particular vertical shower simulation into this Geant4 world. The objective is to quantify the number of particles producing secondary particles following air interactions. The resulting output serves as iterative input for n iterations, where n is determined by the number of Geant4 boxes needed to span the distance L between the detector and the affected zone, as illustrated in Figure 4.3. This relationship is defined by the equation:

$$n = \frac{L}{w} \tag{4.1}$$

where w represents the length of a Geant4 box. This equation helps determine the number of iterations required for the simulation.

For instance, if the initial input consists of N particles and the process yields M particles after n iterations, then M approximates the number of particles the detector would register. So, when simulating the particles with Corsika, it is essential to select an appropriate simulation time for reproducing the particle count at the detector. As previously highlighted, an extended simulated time results in an increased detection of particles (see Annex C1). Establishing the detection zone within a 1 km radius around the detector ensures a significant particle count at the detector.

Chapter V

Results

The development of a method to investigate the impact of seismically induced geo-electromagnetic fields on the detection of secondary cosmic ray fluxes at the Earth's surface has led to insights into the behavior of cosmic ray particles and their interactions within terrestrial environments. This section provides an overview of the relevant results derived from simulations conducted utilizing the Corsika and Geant4 frameworks.

We dedicated significant effort to minimizing the relative error between the two fluxes previously discussed (Φ_S, Φ_G), which represent the primary outcome of all simulations conducted throughout this study. Achieving a reduction in this error signifies the accurate simulation of the Geant4 flux Φ_G within the parameters defined by our project. This accuracy is inferred from its similarity to Φ_S, which is considered the expected or "real" flux, based on Corsika's predictive capabilities.

The primary parameters under discussion encompass a wide array of critical factors, including shower duration, altitude, distance to the detector, particle trajectory length, shower angle, total number of particles generated in Corsika simulations, particles reaching the detection zone,

number of Geant4 boxes employed, length of Geant4 boxes utilized, surviving particles within the Geant4 box, percentage of particle survival, and the frequency of particle injections required into these Geant4 boxes. These parameters are crucial for developing our methodology and will be elucidated through subsequent figures.

These parameters are fundamental to our approach, providing an initial step in our quest to better understand cosmic ray interactions with Earth's atmosphere and the detection process. Detailed analyses of these parameters provide invaluable insights into the efficacy and reliability of our methodology, laying the groundwork for further discussions and interpretations in subsequent sections.

5.1   Simulation parameters and data collection

The simulations comprised a series of computational runs aimed at exploring various parameters crucial for detecting cosmic ray showers. Each run involved varying the parameters defined in Section 4.2.1. These runs were conducted to study the impact of these parameters on the simulated outcomes. The resulting data from each run were meticulously recorded and organized into arrays for subsequent analysis and plotting.

One crucial aspect of the simulations was the determination of simulation time limits. It was noted that standard computers encountered difficulties in running such demanding simulations. The maximum runtime reached, before running out of resources, was 3000 seconds from an initial starting point of 100 seconds. The upper limit of the simulation time was chosen due to the accessible computational power. After several attempts on our machines, we realized that they were able to reach a maximum of 3000 seconds before experiencing failures. Additionally, to assess statistical fluctuations, simulations were repeated with identical parameters, revealing

minimal variations in the final results, typically within a 5.17% margin. This initial attempt paves the way for exploring more efficient methods to simulate additional showers and minimize errors. A glimpse of this progress is depicted in Figure 5.1 with just a few simulation runs.
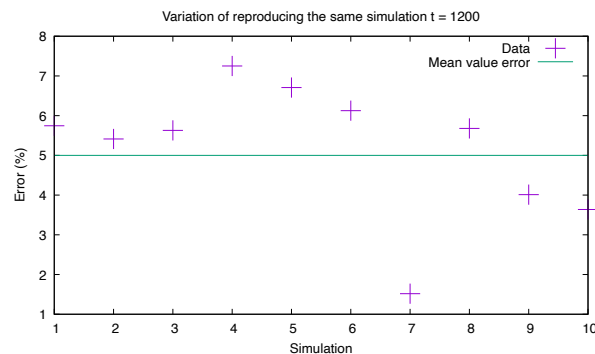

Figure 5.1: Scatter plot depicting the percentage error across 10 runs of identical simulations with consistent parameters: 1200 seconds of shower duration, a distance of 100 km from the detector, and an altitude of 184 km for the affected area. The plot reveals a mean error value of 5%.
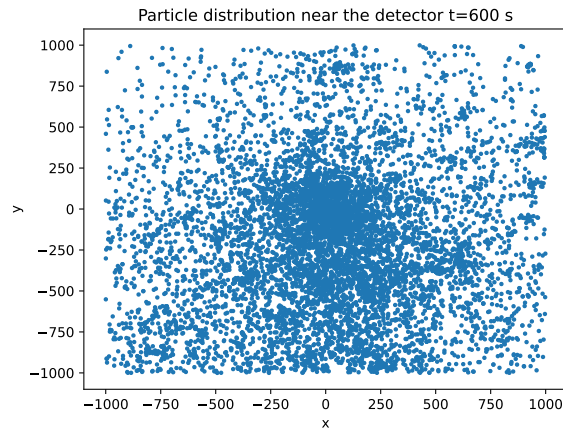
These runs were all identical. Upon analyzing the corresponding code, it was discovered that each time the primary particle flux was generated in ARTI, a random seed was selected. This led to slightly different outcomes for each run while still maintaining the expected particle distribution behavior. The same behavior was observed during the detection process, with particles being filtered near the detector. In this simulation, the average count of filtered particles across all runs was approximately 32,722, with a minimum count of 30,542 particles and a maximum count of 35,465 particles.

Noting that fluctuations in EM fields resulting in variations below 5% in the particle count would be undetectable. Therefore, as previously discussed, more simulations with longer simulation times are necessary, along with significant methodological improvements, our expectation is to reach an error variation of approximately 1%.

As mentioned earlier, increasing the simulation time up to our machine's limits resulted in

a higher particle count and improved statistics, leading to better outcomes when plotting the percentage error versus w. We transitioned from $t = 600$ s, which yielded a particle count in the order of 100,000 particles, to $t = 3000$ s, resulting in a particle count in the order of 10,000,000 particles, as depicted in Figure 5.2.

Furthermore, the maximum duration of particle showers was set to 3000 seconds due to computational limitations in this study. This imposed technical constraints on the scripts associated with the ARTI framework, as detailed in Annex A1.

Particle distribution near the detector t=600 s

(a)

Particle distribution near the detector t=3000 s
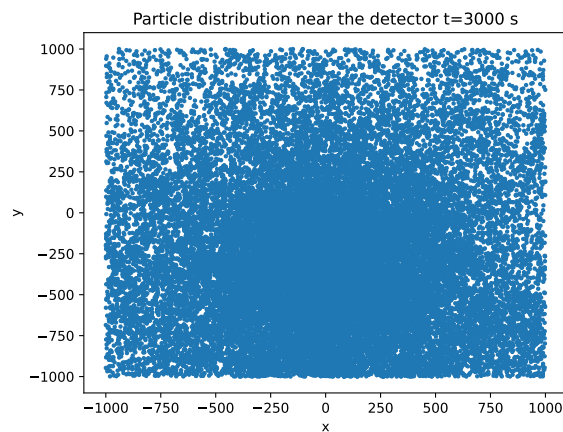
(b)

Figure 5.2: The plot illustrates the particle distribution near the ground at the detector for different simulation times. Panel (a) displays the distribution at 600 s, indicating a lower particle count, while panel (b) shows a significant increase in particle count at 3000 s.

Another important relationship among simulation parameters includes that the altitude of the affected zone, the distance to the detector, and the particle trajectory length. Our initial analysis revealed that the trajectory length L can be approximated as $\sqrt{d^2 + h^2}$. This approximation imposes a constraint on L due to the limited distance d between the affected zone and the detection zone, which is restricted to a range of 500 km before Earth's curvature interferes with

particle detection. Similarly, the upper limit for *h* is determined by earlier studies that have shown significant effects from changes in electromagnetic (EM) fields in the atmosphere up to 300 km above the epicenter.

5.2   Optimization of Geant4 parameters

A significant outcome of this research was the initial attempt to optimize parameters within the Geant4 framework, especially regarding the simulation environment, such as the Geant4 box.

Our initial validation method focused on studying the error behavior related to the Geant4 box length *w* with the aim of finding a tunable function represented as $L = L(w)$ that links this value with the trajectory *L*. This was crucial for determining an optimized *w* value that minimizes the error discussed earlier in this chapter. Note that *L* depends on *h* and *d*, which means that even small changes in *L* require careful calculation to adjust these parameters *h* and *d* across the simulation. While the relationship between them is relatively straightforward, the process of generating and analyzing the simulation was complex. Initially, we set broad limits by simulating very small and very large distances *d*, then gradually narrowed down until every irrelevant particle was excluded from the detection process.

Finding this simplified form of this function would have opened the possibility of discovering a comprehensive function relating all these parameters, such as $L = L(w, d, h, t, \theta)$. This master function would provide optimized values for each desired simulation setup. However, it is important to note that such a function may not even exist or be analytically expressible. Numerous simulations were conducted by varying the values of *L* and *w* accordingly. However, this approach resulted in a highly erratic error distribution concerning *w*, as depicted in some of the initial attempts shown in Figure 5.3.
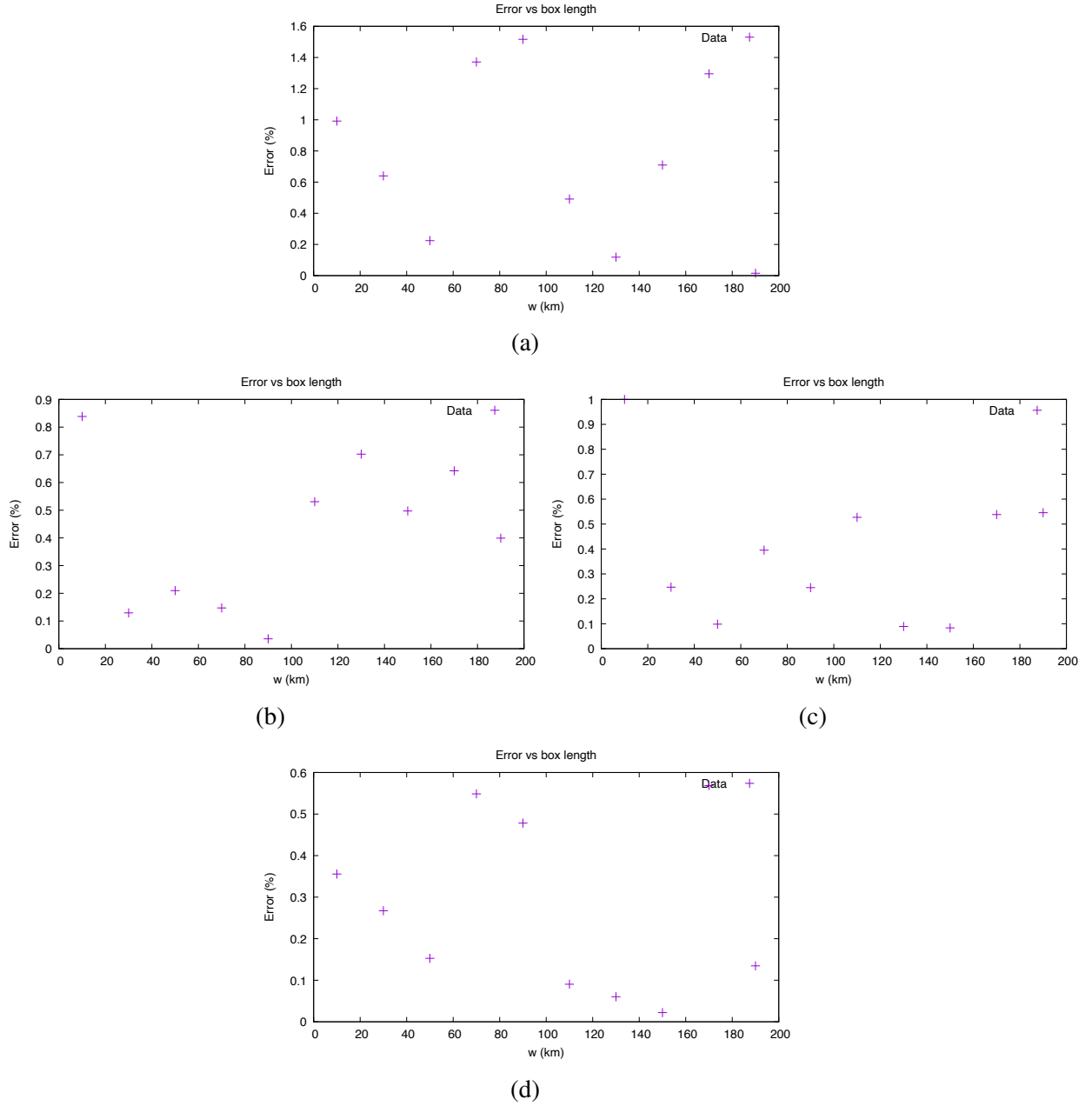
(a)

(b)

(c)

(d)

Figure 5.3: Uncertainty distribution between Φ_S and Φ_G fluxes with respect to different values of $L \in [50, 780]$ and w. It shows a random behavior of the percentage error to the failed proposed tune fuction $L(w)$. In (a) $L = 50$ km, in (b) $L = 123.102$ km, in (c) $L = 196.204$ km, in (d) $L = 269.306$ km. For longer L values, see FigureC1.6

The figure illustrates that our initial approach was suboptimal. We subsequently revised and improved the code, fixing bugs that caused undercounting of particles during filtering after Corsika generation, errors related to neutrons counting, and issues with detection in the logical volume in the Geant4 world. We also increased the statistics by extending simulation time to include more particles, as explained later, resulting in more manageable and accurate results. Nevertheless, there remains significant room for improvement in future studies concerning these parameters. Moreover, analyzing statistical data from numerous simulations provided insights into how the duration of showers affects the reliability of results. Short simulation times, common in local machine simulations, showed results sensitive to variations caused by effects that could be merely random fluctuations, as well as by other unknown phenomena that could obscure any impact of electromagnetic (EM) fields and thus their measurement. Extending the simulation time increased the number of particles reaching the filtered or detected zone, thereby reducing counting fluctuations. This feature highlights the significance of simulating realistic time durations to minimize the impact of EM field variations, as discussed in Annex C1.

As depicted in Figure 5.3 above, many aspects of our approach were suboptimal. However, this insight is invaluable for future research in this field as it provides guidance for optimizing Geant4 parameters like box length or diameter. Attempting to establish an explicit correlation function with an external parameter such as the total particle trajectory L was not feasible given the available computational power. To constrain the optimized values of each parameter introduced in this phase of the project, it is advisable to conduct longer duration runs of the same simulation. This approach reduces error bars, allowing for thorough analysis of statistical fluctuations and the exclusion of other potential effects. Through extensive data collection, achieved by running numerous simulations using the tools outlined in AnnexA1 and A2, it may be possible to discover a correlation function that can be properly optimized as needed.

These were first-generation code revisions, and additional revisions not only to the code but also to all the software needed may lead to better results.

Following the refinement of the unsuccessful approach by redefining the tuning function for the parameters, debugging the code, and conducting similar simulations with the same simulation time and affected zone altitude but at larger distances (thus larger values of L), it was observed that when running these different L values, the optimal length of the Geant4 box averages 10 $\pm 2\%$ of the total path length of particles, as depicted in Figure 5.4.
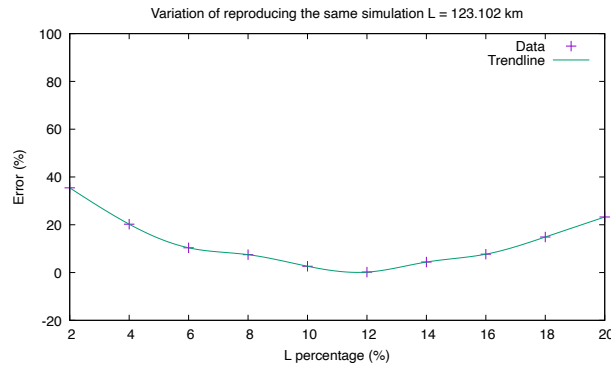
(a)
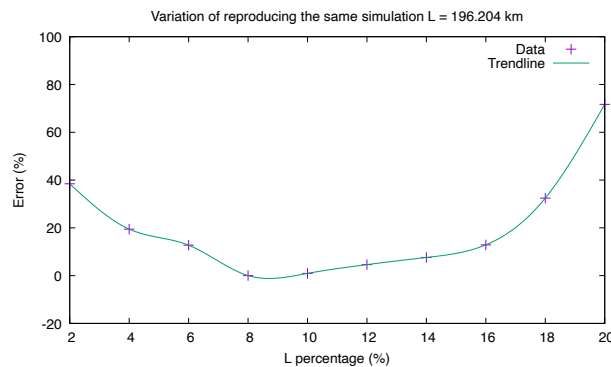
(b)

Figure 5.4: The plot shows results from 10 runs of two similar simulations, each conducted for 1200 seconds with a 100 km altitude of the affected zone but at different distances d. In (a), the minimum error value was observed when using $w = 12\%$ of L, while in (b), the minimum error value was obtained for $w = 8\%$ of L.

This estimation takes into account the square root of the sum of the squared distance and altitude, providing an approximation of the effective path length traveled by the particles. it is important to note that this is an initial estimate and can be further refined through ongoing work on this project. This optimization ensures a balance between computational efficiency and accuracy in simulating particle interactions within the designated volume.

5.3 Script development and workflow

In addition to the generation of valuable simulation data, this research facilitated the development of scripts tailored to streamline simulation processes and data analysis. These scripts enhanced the efficiency and reproducibility of the simulation workflow, enabling researchers to conduct systematic investigations with greater ease and accuracy. By automating repetitive tasks and standardizing analysis procedures, these scripts contribute to the advancement of cosmic ray detection methodologies and facilitate further research in this field.

The scripts are readily available in the GitHub repository dedicated to this study [42], along with detailed information on their functionality. The pseudocode for both main scripts is explained in Annex A2. Instructions on effectively using and running them are provided in Annex A1 and Annex A2, respectively.

Furthermore, for a more streamlined approach to access all the software used in this study, including obtaining the Docker container that encapsulates everything [41], the instructions are the same as those outlined in Annex A1 and Annex A2.

Chapter VI

Conclusions

In this work, we study the feasibility of developing a method that will eventually help us understand how seismically induced geo-electromagnetic fields impact the detection of secondary particles on Earth's surface. We implemented a strategy involving different software frameworks, key parameters, and a first attempt at particle flux analysis in this context. We were able to indicate, within limitations, initial constraints on several parameters required for generating the data.

In our preliminary simulations, we faced specific constraints regarding simulation parameters. For example, we set boundaries on the distance between the affected and detection zones (d) and the altitude of the affected zone (h) as $d < 500$ km and $h < 300$ km, respectively. These limitations led to an overarching constraint on the total particle length (L), whereby $L < 580$ km.

At first, our study covered simulation times ranging from 100 to 3000 seconds. However, through script modifications, we expanded the upper time limit. This improvement enables a more extensive utilization of simulation time when using the software customized for this study

(provided sufficient resources are available).

Optimizing Geant4 parameters, such as simulation duration and box length, notably improved result reliability and accuracy. Tuning these parameters allows future researchers to balance computational efficiency and simulation realism, enhancing cosmic ray simulations' fidelity in this study. While attempting to find a master function for all parameters, we found this approach unfeasible. However, increasing statistics with larger shower durations reduced fluctuations. Setting the Geant4 box length as $w = 10\% \pm 2\%$ of L notably reduced percentage error, although further improvements are necessary for error reduction and precise w description.

The streamlined software workflows, with simulation generation and data analysis scripts, greatly boosted research productivity and reproducibility. These tools support systematic investigations and simplify data analysis. Facing challenges with local machine simulations, we resolved this by using Docker containers for software access independent of computational power.

Extending simulation time increases particles at the detection zone, enhancing statistical significance with a larger dataset. Despite decreasing counts with distance, more particles are beneficial. Scaling time is crucial for adequate counts, and we found a linear relationship for generating desired particle numbers with specified simulation time. This is vital for optimizing resources in larger simulations.

This study highlights the importance of thorough simulation methods and optimization in advancing cosmic ray understanding. Using advanced computational techniques and statistical analyses, we've made significant progress in unraveling cosmic ray interactions, paving the path for future breakthroughs.

Finally, for future work in this field, meticulous attention should be paid to simulating ARTI particles and LAGO sites with greater precision, especially when correlating simulation re-

sults with actual physical detector counts. Other improvements could include modifying the particle filtering area to extend beyond 1 km around the detector, although this parameter is currently fixed in the code. Additionally, improvements in Geant4's particle tracking to reduce grid granularity and create larger detection paths are necessary, as the current milimetric granularity increases memory storage exponentially, making it inefficient. Furthermore, providing a Docker container with all the specifications outlined in this work will allow future researchers to construct a manageable workflow capable of creating data for any location and desired electromagnetic field variation.

References

[1] *What are cosmic rays?* `https://news.uchicago.edu/explainer/what-are-cosmic-rays`. Accessed: 15/03/2024.

[2] Antoine Letessier-Selvon and Todor Stanev. "Ultrahigh energy cosmic rays". In: *Reviews of Modern Physics* 83.3 (Sept. 2011), pp. 907–942. ISSN: 1539-0756. DOI: `10.1103/revmodphys.83.907`. URL: `http://dx.doi.org/10.1103/RevModPhys.83.907`.

[3] V. L. Ginzburg and S. I. Syrovatskii. *The Origin of Cosmic Rays*. 1964.

[4] W. I. Axford, E. Leer, and G. Skadron. "The Acceleration of Cosmic Rays by Shock Waves". In: *International Cosmic Ray Conference*. Vol. 11. International Cosmic Ray Conference. Jan. 1977, p. 132.

[5] G. F. Krymskii. "A regular mechanism for the acceleration of charged particles on the front of a shock wave". In: *Akademiia Nauk SSSR Doklady* 234 (June 1977), pp. 1306–1308.

[6] A. R. Bell. "The acceleration of cosmic rays in shock fronts – I". In: *Monthly Notices of the Royal Astronomical Society* 182.2 (Feb. 1978), pp. 147–156. ISSN: 0035-8711. DOI: `10.1093/mnras/182.2.147`. eprint: `https://academic.oup.com/`

`mnras/article-pdf/182/2/147/3710138/mnras182-0147.pdf`. URL: `https://doi.org/10.1093/mnras/182.2.147`.

[7]   Roger Blandford and David Eichler. "Particle acceleration at astrophysical shocks: A theory of cosmic ray origin". In: *Physics Reports* 154.1 (1987), pp. 1–75. ISSN: 0370-1573. DOI: `https://doi.org/10.1016/0370-1573(87)90134-7`. URL: `https://www.sciencedirect.com/science/article/pii/0370157387901347`.

[8]   *Primary Cosmic Ray*. `https://www.sciencedirect.com/topics/chemistry/primary-cosmic-ray`. Accessed: 15/03/2024.

[9]   H. H. Mielke et al. "Cosmic ray hadron flux at sea level up to 15-TeV". In: *J. Phys. G* 20 (1994), pp. 637–649. DOI: `10.1088/0954-3899/20/4/010`.

[10]   Todor Stanev. "High energy interactions and extensive air showers". In: vol. 516. Jan. 2000, pp. 247–261. DOI: `10.1063/1.1291479`.

[11]   G. B. Yodh et al. "Proton-proton cross sections from 1 to 100 TeV". In: *Phys. Rev. D* 27 (5 Mar. 1983), pp. 1183–1186. DOI: `10.1103/PhysRevD.27.1183`. URL: `https://link.aps.org/doi/10.1103/PhysRevD.27.1183`.

[12]   T. K. Gaisser, U. P. Sukhatme, and G. B. Yodh. "Hadron cross sections at ultrahigh energies and unitarity bounds on diffraction". In: *Phys. Rev. D* 36 (5 Sept. 1987), pp. 1350–1357. DOI: `10.1103/PhysRevD.36.1350`. URL: `https://link.aps.org/doi/10.1103/PhysRevD.36.1350`.

[13]   M. Honda et al. "Inelastic cross section for p-air collisions from air shower experiments and total cross section for p-p collisions up to $\sqrt{s}$ =24 TeV". In: *Phys. Rev. Lett.* 70 (5

Feb. 1993), pp. 525–528. DOI: 10.1103/PhysRevLett.70.525. URL: https://link.aps.org/doi/10.1103/PhysRevLett.70.525.

[14] R. M. Baltrusaitis et al. "Total Proton-Proton Cross Section at $s^{\frac{1}{2}} = 30$ TeV". In: *Phys. Rev. Lett.* 52 (16 Apr. 1984), pp. 1380–1383. DOI: 10.1103/PhysRevLett.52.1380. URL: https://link.aps.org/doi/10.1103/PhysRevLett.52.1380.

[15] EAS-Top Collaboration et al. "Study of jet production in p-N interactions at sqrt(s)~500 GeV in EAS multicore events". In: *Physics Letters B* 460.3-4 (Aug. 1999), pp. 474–483.

[16] N.N. Kalmykov, S.S. Ostapchenko, and A.I. Pavlov. "Quark-gluon-string model and EAS simulation problems at ultra-high energies". In: *Nuclear Physics B - Proceedings Supplements* 52.3 (1997), pp. 17–28. ISSN: 0920-5632. DOI: https://doi.org/10.1016/S0920-5632(96)00846-8. URL: https://www.sciencedirect.com/science/article/pii/S0920563296008468.

[17] P.K.F. Grieder. *Cosmic Rays at Earth*. 1st ed. 2001. ISBN: 9780444507105. URL: libgen.li/file.php?md5=d0af831816e7b48868dd0f68c142a1db.

[18] S. Buitink et al. "Monte Carlo simulations of air showers in atmospheric electric fields". In: *Astroparticle Physics* 33.1 (Feb. 2010), pp. 1–12. DOI: 10.1016/j.astropartphys.2009.10.006. URL: https://doi.org/10.1016%2Fj.astropartphys.2009.10.006.

[19] 2018 Yongxin Gao. et al. "Induced electromagnetic field by seismic wave in earth's magnetic field: a 2D layered case ". In: Poster presented at International Symposium on Eartquake Forecast / 5th International Workshop on Earthquake preparation process (ISEF-IWER5), Chiba, Japan.

[20] Jianfeng Su and Hai Chen. "Study on the mechanism of atmospheric electric field anomalies before earthquakes". In: *Results in Geophysical Sciences* 15 (2023), p. 100060. ISSN: 2666-8289. DOI: `https://doi.org/10.1016/j.ringps.2023.100060`. URL: `https://www.sciencedirect.com/science/article/pii/S266682892300010X`.

[21] Yongxin Gao et al. "Induced electromagnetic field by seismic waves in Earth's magnetic field". In: *Journal of Geophysical Research: Solid Earth* 119.7 (2014), pp. 5651–5685. DOI: `https://doi.org/10.1002/2014JB010962`. eprint: `https://agupubs.onlinelibrary.wiley.com/doi/pdf/10.1002/2014JB010962`. URL: `https://agupubs.onlinelibrary.wiley.com/doi/abs/10.1002/2014JB010962`.

[22] Xuemin Zhang et al. "Ground-based and satellite DC-ULF electric field anomalies around Wenchuan M8.0 earthquake". In: *Advances in Space Research* 50 (July 2012), pp. 85–95. DOI: `10.1016/j.asr.2012.03.018`.

[23] Zhong Li et al. "Study on VLF Electric Field Anomalies Caused by Seismic Activity on the Western Coast of the Pacific Rim". In: *Atmosphere* 14.11 (2023). ISSN: 2073-4433. DOI: `10.3390/atmos14111676`. URL: `https://www.mdpi.com/2073-4433/14/11/1676`.

[24] Yoshimori Honkura and Yuri Kuwata. "Estimation of electric fields in the conducting Earth's crust for oscillating electric current dipole sources and implications for anomalous electric fields associated with earthquakes". In: *Tectonophysics* 224.1 (1993), pp. 257–263. ISSN: 0040-1951. DOI: `https://doi.org/10.1016/0040-1951(93)`

90078-X. URL: `https://www.sciencedirect.com/science/article/pii/004019519390078X`.

[25] Ronnie Jansson and Glennys R. Farrar. "A NEW MODEL OF THE GALACTIC MAG-NETIC FIELD". In: *The Astrophysical Journal* 757.1 (Aug. 2012), p. 14. ISSN: 1538-4357. DOI: `10.1088/0004-637x/757/1/14`. URL: `http://dx.doi.org/10.1088/0004-637X/757/1/14`.

[26] Andrii Neronov and Ievgen Vovk. "Evidence for Strong Extragalactic Magnetic Fields from Fermi Observations of TeV Blazars". In: *Science* 328.5974 (Apr. 2010), pp. 73–75. ISSN: 1095-9203. DOI: `10.1126/science.1184192`. URL: `http://dx.doi.org/10.1126/science.1184192`.

[27] *Earth's Magnetosphere*. `https://science.nasa.gov/science-research/planetary-science/earths-magnetosphere/`. Retrieved from NASA website. 2023.

[28] A. Buchachenko. "Self-Excitation of the Earthquake". In: *Open Journal of Earthquake Research* 11 (2022), pp. 18–30.

[29] George Winfred Moore. "Magnetic Disturbances preceding the 1964 Alaska Earthquake". In: *Nature* 203 (1964), pp. 508–509. URL: `https://api.semanticscholar.org/CorpusID:4215939`.

[30] Yongxin Gao et al. "On magnetic disturbances induced by rotation of coil-type magnetometer driven by seismic waves". In: *Geophysical Journal International* 226.3 (May 2021), pp. 1948–1974. ISSN: 0956-540X. DOI: `10.1093/gji/ggab190`. eprint: `https://academic.oup.com/gji/article-pdf/226/3/1948/`

`38496440 / ggab190 . pdf.` URL: `https : / / doi . org / 10 . 1093 / gji / ggab190.`

[31] Dieter Heck et al. "Corsika: A Monte Carlo code to simulate extensive air showers". In: *Forschungszentrum Karlsruhe* (1998).

[32] *About (LAGO) The Latin American Giant Observatory*. `https : / / lagoproject . net / about / about . html.` Accessed: 22/04/2024.

[33] Christian Sarmiento-Cano et al. "The ARTI framework: cosmic rays atmospheric background simulations". In: *The European Physical Journal C* 82.11 (Nov. 2022). ISSN: 1434-6052. DOI: `10.1140/epjc/s10052-022-10883-z.` URL: `http://dx. doi.org/10.1140/epjc/s10052-022-10883-z.`

[34] Stefano Agostinelli et al. "Geant4—A Simulation Toolkit". In: *Nuclear Instruments and Methods in Physics Research Section A: Accelerators, Spectrometers, Detectors and Associated Equipment* (Oct. 2003). Geant4 Collaboration. DOI: `10 . 1016 / s0168-9002(03)01368-8.` URL: `https://doi.org/10.1016%2Fs0168-9002% 2803%2901368-8.`

[35] J. Allison et al. "Recent developments in Geant4". In: *Nuclear Instruments and Methods in Physics Research Section A: Accelerators, Spectrometers, Detectors and Associated Equipment* (Nov. 2016). Geant4 Collaboration. DOI: `10.1016/j.nima.2016.06. 125.` URL: `https://doi.org/10.1016%2Fj.nima.2016.06.125.`

[36] Katsuya Amako et al. "Geant4—a simulation toolkit". In: *Nuclear Instruments and Methods in Physics Research Section A: Accelerators, Spectrometers, Detectors and Associated Equipment* (Aug. 2015). Geant4 Collaboration. DOI: `10.1016/j.nima.2015. 04.064.` URL: `https://doi.org/10.1016%2Fj.nima.2015.04.064.`

[37] D. Heck et al. *CORSIKA User's Guide*. 1998. URL: `https://www.ikp.kit.edu/corsika/users-guide/users-guide.pdf`.

[38] CERN. *Geant4 Documentation*. URL: `https://geant4.web.cern.ch/docs/`.

[39] Pablo Buitrón. *Algoritmo para correr simulaciones*. 2023. URL: `https://github.com/pablobuitron/masterthesis/issues/30`.

[40] Pablo Buitrón. *Inconvenientes con "Build and Install" de Geant4*. 2023. URL: `https://github.com/pablobuitron/masterthesis/issues/38`.

[41] Pablo Buitrón. *Docker Container with software needed for shower simulation and analysis with Geant4*. 2023. URL: `https://hub.docker.com/r/pablobuitron/autotry`.

[42] Pablo Buitrón. *Masther Thesis GitHub Project*. 2023. URL: `https://github.com/pablobuitron/masterthesis`.

ANNEX A1: Procedure for Generating ARTI Particle Table

1. Download the Docker image using `docker pull pablobuitron/autotry:latest`

   To use this script, it is necessary to first obtain the Docker image in which both ARTI and the required version of Corsika are already installed.

2. Set up a Docker container using this image.

   It is necessary to create the container with `-v` by mounting a volume in the host machine to the `/home` directory in the container. This volume is where all the outputs of each simulation will be saved. Also, use the `-it` flag to actually access it and run the next commands.

3. Modify the input file named `datos.txt`.

   This file is located in the working directory of the Docker container, i.e., in the directory `/opt/`. It will have as many rows as simulations are desired. It consists of 4 columns separated by a tab and follows this order: `t` `d` `h` θ , where `t` is the shower time to be simulated, `d` is the distance from the detector to the earthquake epicenter, `h` is the

height of the affected zone generated by the earthquake, and θ is the angle of the shower required. This last parameter limits the rain region that will pass through the affected zone, as visualized in Figure 4.1.

Note: Running identical simulations with the same parameters will overwrite the information. Always vary at least slightly either the shower time or the angle to change the output names.

4. Run the simulations using `./tesisauto.sh`.

   Once the `datos.txt` file has been modified with the required simulations and their respective parameters, simply run the command line `./tesisauto.sh` in the directory `/opt/`.

Note: Running all simulations may take hours, depending on the shower times set for each one, and the particle filtering and analysis must also be processed.

5. Review the results.

   Access the directory where the container was mounted and review the created files. There should be files with the name of the respective simulation filtered by particles, an image showing the particle dispersion near the detector, and a `.shw.bz2` file containing all the information that will be later introduced into the analysis with the Geant4 world.

ANNEX A2:Injecting the table into Geant4 and Data Analysis

1. Locate the `.shw.bz2` file.

   This file is automatically copied to the Geant4 simulation directory, which is `/opt/fsim/build/`

2. Run the simulation `./sim -m input.in > run.log`.

   This command should be run in the directory `/opt/fsim/build/`. This is where the Geant4 simulation lives and compiles, injecting the particles obtained previously.

3. Analyze and count surviving particles.

   All surviving particles that pass through the air-filled cylinder will be found in the `run.log` file. This percentage of surviving particles will be known as the survival rate.

Note: The current container does not have Geant4 installed, but future versions will have it, and the complete simulation and analysis flow can be performed there.

ANNEX B1: Pseudocode Scripts for Data Analysis

The following scripts, along with a more detailed explanation, can be found in [42].

Algorithm 1 `newfilter.py` Pseudocode

1: Import the necessary libraries: pandas for data handling and matplotlib.pyplot for plotting.

2: Set the simulation parameters such as minimum angle, maximum angle, and distance from the detector to the epicenter.

3: Read data from a CSV file into a pandas DataFrame.

4: Filter the data based on how close we want particles to be arround the detector.

5: Count the number of particles that pass the filter.

6: Write the count of particles to a text file.

7: Create a scatter plot of the filtered data using matplotlib.

8: Save the scatter plot as an image file.

9: Save the filtered data to a text file.

Algorithm 2 `tesis.sh` Pseudocode

1: Initialize variables:

2: Set base directory.

3: Set input data file path.

4: Set Corsika directory.

5: Set result directory.

6: Set output file path.

7: Set Geant4 directory.

8: Set column separator in data file to tab character

9: Open input data file for reading

`tesis.sh` Pseudocode (continued)

1: **while** there are lines to read in the data file **do**
2:     Read a line from the data file
3:     Extract time, height, distance, and angle from the line
4:     Split the line using tab character as the separator
5:     Assign values to time, height, distance, and angle variables
6:     Run simulations:
7:     Change directory to the base directory
8:     Execute the simulation script `do_sims.sh` with specified parameters
9:     Sleep for 7 seconds (to allow simulation to start)
10:    Change directory to the Corsika directory
11:    Run the polarization restriction script based on the time format
12:    Sleep for 15 seconds (to allow process to finish)
13:    Run the `rungo.sh` script based on the time format
14:    Wait for simulation processes to finish:
15:    Wait until the Corsika and bzip2 processes are not running
16:    Process simulation results:
17:    Change directory to the base directory
18:    Execute the result processing script `do_showers.sh` with specified parameters
19:    Sleep for 60 seconds (to allow process to finish)
20:    Copy compressed result files to the Geant4 and result directories
21:    Decompress result files in the result directory
22:    Modify result files to remove headers and extract relevant data
23:    Obtain particle count and filter data using the `newfilter.py` script
24:    Update the output file with processed data:
25:    Append filtered particle count and total particle count to the output file
26: **end while**

ANNEX C1: Correlation Plots for Simulation Parameters

FigureC1.1 shows the relationship between the number of surviving particles in the Geant4 world and the shower duration. As expected, there is a positive correlation between these two variables, indicating that longer shower durations result in a higher number of surviving particles reaching the detection zone.

The tendence line represents the linear regression fit, which can be expressed as:

$$\Phi_G = at + b$$

Where Φ_G is the number of surviving particles normalized to unit area and time, t is the shower duration, and a and b are the slope and intercept of the regression line, respectively. The values of a and b obtained from the fit are provided in the figure caption.

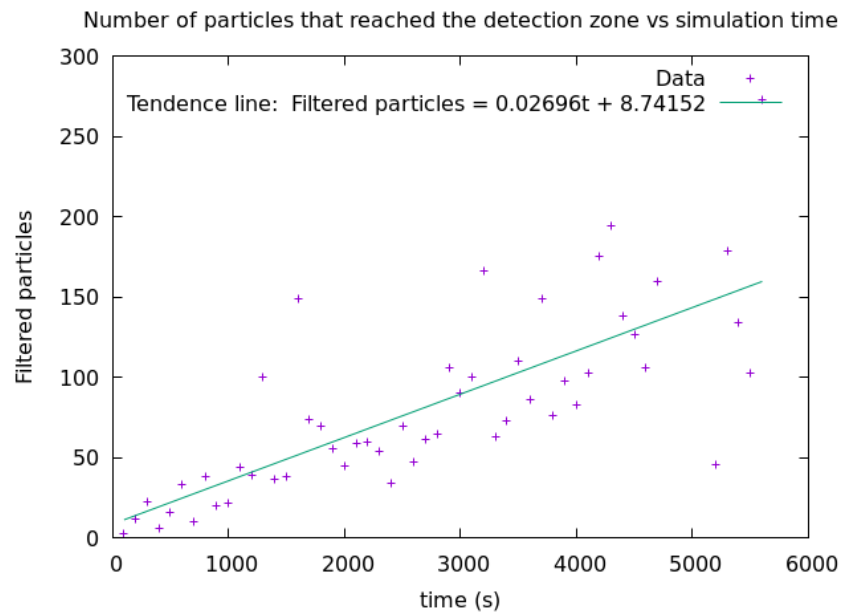Number of particles that reached the detection zone vs simulation time

Figure C1.1: Scatter plot of the number of surviving particles in the Geant4 world versus shower duration. The tendence line is the linear regression fit with slope a = 0.02696 particles/second and intercept b = 8.74152 particles.

This plot, as well as the subsequent ones, were generated with fixed parameters: the distance to the detector set at $d = 100$, the altitude of the affected area at $h = 100$, and a lower limit angle for the shower of $\theta = 20$.
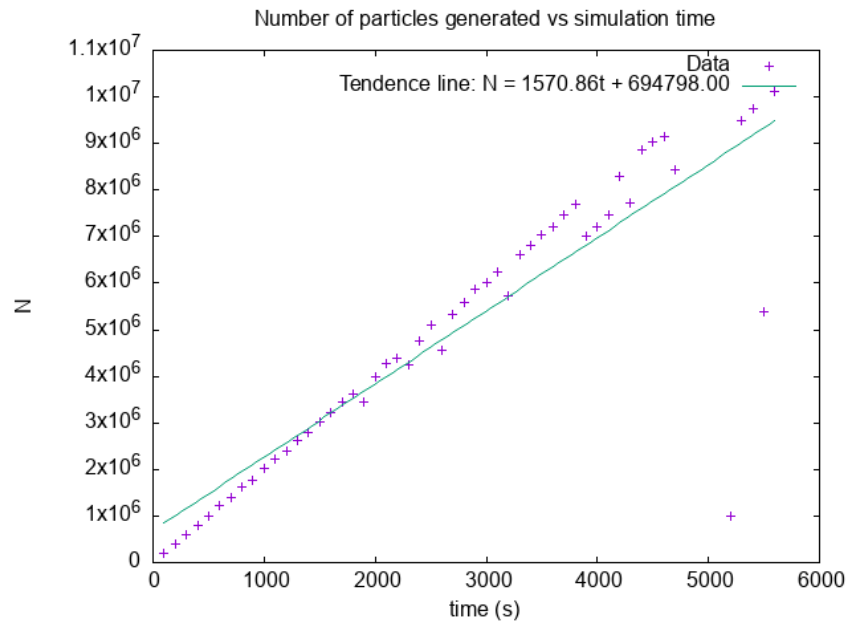
Figure C1.2: Scatter plot of the number of total generated particles in the Corsika versus shower duration. The tendence line is the linear regression fit with slope a = 1570.86 particles/second and intercept b = 694798 particles.

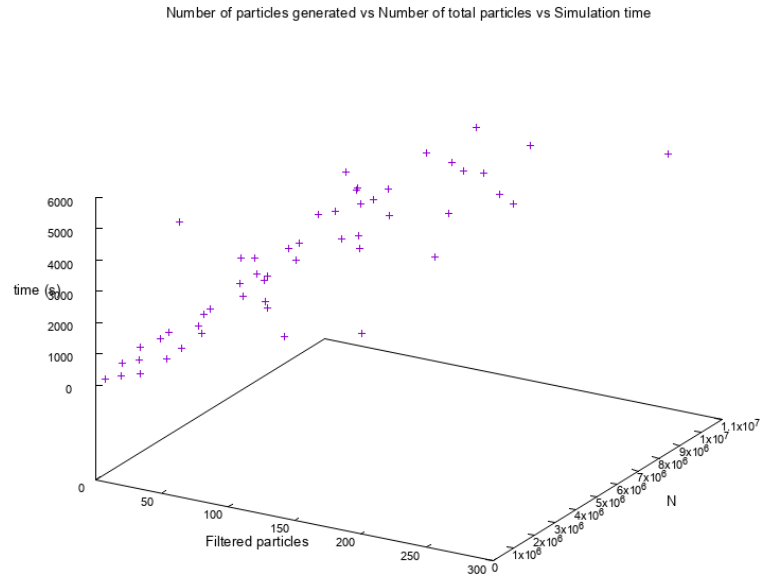Number of particles generated vs Number of total particles vs Simulation time

Figure C1.3: Scatter plot of the number of total generated particles in the Corsika versus Filtered particles versus shower duration.

Figure C1.4 shows the relationship between the number of surviving particles and the distance to the detector. As the distance increases, the number of surviving particles decreases due to particle attenuation during propagation through the atmosphere. The relationship appears to follow an exponential decay, which can be described by the equation:

$$N_{surv} = N_0 e^{-\lambda d}$$

Where N_0 is the initial number of particles, d is the distance to the detector, and λ is the attenuation coefficient. The fitted curve is shown as a dashed line in Figure 2, with the value of λ provided in the figure caption.
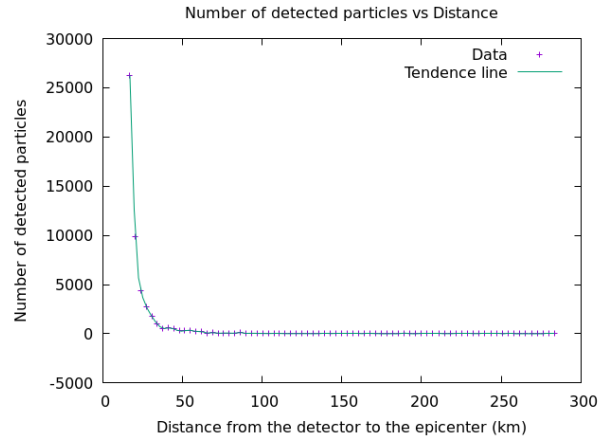
Figure C1.4: Scatter plot of the number of surviving particles in the Geant4 world versus distance to the detector. The solid line represents the exponential decay fit with attenuation coefficient $\lambda = 0.153 \ \mathrm{km}^{-1}$.

This plot, as well as the following one, were generated with a fixed simulation time at $t = 1200$ s while varying the distance and altitude to observe changes in detection.
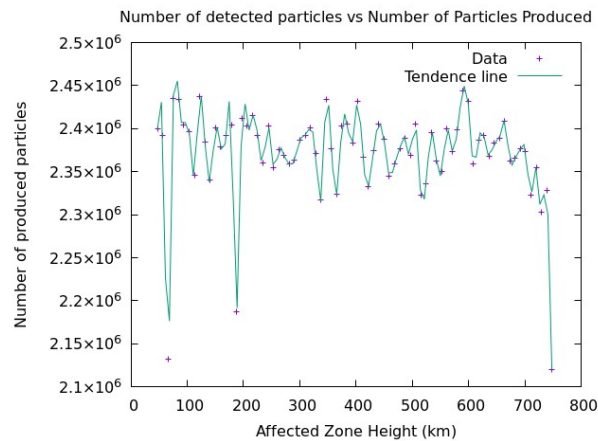

Figure C1.5: Scatter plot of the number of generated particles versus altitud of the affected zone.
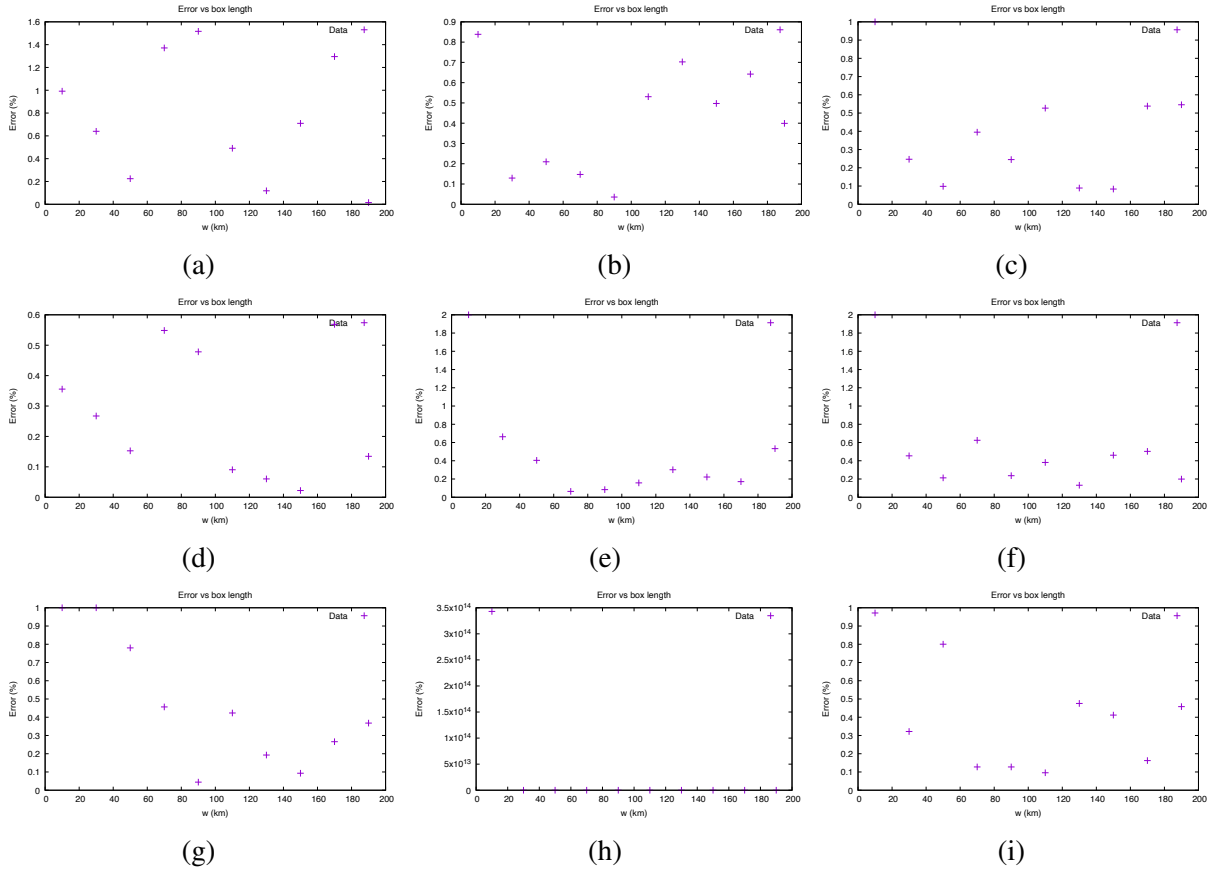
Figure C1.6: Error distribution with respect to different values of $L \in [50, 780]$ and $w \in [10, 190]$

This figure illustrates the erratic behavior of the percentage error when varying w using low simulation time and, consequently, a low particle count.